Experimental Determination of Hydrogen-Air Laminar Burning Velocities, and the Effect of Water Mist

Wulme Puoru Dery

A thesis in partial fulfilment of the requirements for the degree of *Master of Science* in the subject of Physics Process Safety Technology

University of Bergen, Department of Physics and Technology

Abstract

This research project characterises an experimental set-up with the aim of finding laminar burning velocities of premixed hydrogen-air (dry) mixtures, at initial pressure and pressure of 294 K and 1 bar, using a 20 litre cubic explosion chamber.

Two different methods were employed; a constant-pressure method (CPM) applied with a schlieren imaging technique, and a constant-volume method (CVM) adopting the pressure-time history. Regarding the former method, linear and non-linear relation between the propagation of flame and stretch rate was employed to obtain the unstretched flame and burning velocity. Using the pressure measurements during the transient dispersion process, CPM using a pressure transducer was employed to calculate the burning velocity, relating the pressure rise to the radius of the flame.

Both measuring techniques gave laminar burning velocities in agreement, with a maximum relative difference of 10 %. Observed wrinkling in the flame propagation due to hydrodynamic instabilities, in addition to limitations associated with experiments performed in a cubical vessel, made it difficult to produce quantitative results unison with those found in other literature.

Using a nozzle, hydrogen-air mixtures were introduced to water mist with concentrations between 0.08-0.3 m^3/kg. This was done to investigate its influence on the laminar burning velocity. The inclusion of water mist gave burning velocities increased with as high as 100 %, compared to the dry results. This was mainly due to the generation of turbulence during the injection of water mist.

Preface

This is a Master's thesis submitted as part of a Master of Science degree in the subject of Process Safety Technology at the Department of Physics and Technology (DPT) at the University of Bergen. The experimental work was carried out in the Bjørn Trumpy House belonging to DPT, and in cooperation with the company Gexcon AS. The work started in the fall of 2016 and was completed in June 2017.

Acknowledgements

First of all, I would like to thank the University of Bergen for enabling me the opportunity to conduct an experimental research thesis, and also to Gexcon AS for the cooperation in implementing it. As with most research projects, obstacles along the way is presumably inevitable. Fortunately, I have had many able minds to turn to along the way:

My supervisors Bjørn Arntzen and Morten Holme for excellent guidance, and enduring feedback during the entire process, Kari Halland for initially showing me around the lab, Werner Olsen for assistance in making and understanding the electronic equipment, Roald Langøen and Charles Sebastiampillai for exceptional work done in the mechanical workshop constructing and modifying apparatus used, Rachid Maad for helping install the LabVIEW-software needed, Yi-Chun Chen for help understanding the optical system and lending me lenses, Laurence Benhard for assisting in fine-tuning the optical system and Andre Vagner Gaathaug for welcoming me to observe their schlieren set-up at the University College in Telemark.

My fellow classmates with whom I shared an office with, and otherwise encountered regularly during this period has been immensely cherished. The comradely atmosphere, may it be during lunch (s/o Tran Hieu Thi) or playing fooseball will not be forgotten, and friendships made assuredly preserved. I'd also like to thank those along the way who provided dank memes (Philippe, Andre, Sindre), supplied with good music (Ebro), and proofread (Jon, Tone, Marcus). Last but not least, I'd like to thank my parents for endless love, support and encouragement, and my brother for just being there.

> *"I think it's possible to learn. The problem is that we learn so damned slowly, so that by the time you've realized something, it's too late." - Harry Hole*

Contents

List of Figures

List of Tables

Nomenclature

Abbreviations

BNC	Bayonet Neill-Concelman
CEC	Chemical Equilibrium Calculator
CPM	Constant-Pressure Method
CVM	Constant-Volume Method
DPT	Department of Physics and Technology
FLACS	FLame ACceleration Simulator
FPS	Frames Per Second
LFL	Lower Flammability Limit
PFV	Photron Fastcam Viewer
SMD	Sauter Mean Diameter
UFL	Upper Flammability Limit
UoB	University of Bergen

Other Symbols

ϕ	Equivalence ratio
$f/number$	Focal ratio
n_{air}	Mole fraction of air in mixture
n_{fuel}	Mole fraction of fuel in mixture
$vol\%$	Volume percent
vol_{fuel}	Volume fraction of fuel in mixture
vol_{total}	Total volume of gas mixture

Latin and Greek Symbols

α	Stretch rate	1/s
γ	Specific heat ratio	
ρ_b	Density of burned gas	kg/m^3
ρ_u	Density of unburned gas	kg/m^3
ξ	Light refraction angle	
A	Flame surface area	m^2
C	Capacitance	F
c	Speed of light in vacuum	m/s

C_p	Specific heat capacity at constant pressure	J/(kg K)
C_v	Specific heat capacity at constant volume	J/(kg K)
D	Diameter	mm
E	Energy stored in a capacitive spark	J
E	Expansion ratio	
f	Focal length	mm
K	K-factor	l/(min bar)
k	Gladstone-Dale coefficient	cm^3/g
L	Markstein length	mm
n	Number of moles	
n	Refractive index	
p	Pressure	bar
p_i	Initial pressure	bar
$p_{max,ad}$	Adiabatic isochoric equilibrium combustion pressure	bar
p_{max}	Maximum explosion pressure	bar
p_{nozzle}	Water pressure on the nozzle	bar
R	Gas constant	J/(K mol)
r_f	Flame radius	m
R_s	Specific gas constant	J/(K kg)
R_v	Radius of the vessel	m
S_f	Flame speed	m/s
S_g	Unburned gas flow velocity	m/s
S_u	Laminar burning velocity	m/s
S_{u_0}	Burning velocity at initial reference conditions	m/s
T	Temperature	K
t	Time	s
U	Voltage	V
V	Volume	m^3
v	Light speed in a medium	m/s

Chapter 1

Introduction

1.1 Motivation

The leading objective of this thesis is to experimentally obtain laminar burning velocities, a fundamental input parameter necessary to simulate dispersion and/or gas explosions, with particular spotlight on scenarios whereby water mist is present.

The aim, together with the Safety Technology subgroup within the Process Technology group at the Department of Physics and Technology (DPT), is to focus on safety technology and combustion phenomena. To acquire research-based knowledge about various parameters related to combustion and explosion hazards especially on gas and dust explosion [1]. Both experimentally and numerically, research tasks are often collaborated with external agencies, such as Gexcon, one of the leading research environments in the world in the field of gas explosions. To investigate parameters associated with explosions, Gexcon carries out safety assessments, research projects and physical testing of gases and dusts including part taken in investigations of large accidents like Piper Alpha in 1988 and the Texas City refinery in 2005 [2].

Gexcon develops, maintains and uses the industry standard software for modelling gas explosions; FLame ACceleration Simulator (FLACS). As a computational fluid dynamics tool, the software can be used in full 3D for all typical flammable and toxic release scenarios predicting consequences much more accurately and including effects of all contributing and mitigating effects such as confinement and congestion due to existent geometry, ventilation

and deluge [2]. The software became commercially available in the 1990s, and to meet the requests from the industry, continuous development and maintenance is necessary. In cases whereby little to no accredited literature data is available for input parameters for various gases in the FLACS software relating to combustion, an effort to locally obtain these values is applied. The laminar burning velocity in particular, is an important mixture property and is extensively used in extracting information about diffusivity and reactivity for any given fuel-air mixture [3].

With regards to this, in recent years the term "hydrogen economy" has experienced a spike in attention due to its potential as an energy carrier, transitioning the use of fossil-fuel-based energy to a more sustainable one [4]. Hydrogen, despite being one of the most common chemical element, does not exist in nature in its pure form. It has to be separated from hydrocarbons or other hydrogen carriers, either by electrolysis from water or by chemical processes. Both these instances of hydrogen formation may occur in a nuclear power plant, either as part of normal operations, or following a severe accident [5]. Hydrogen has a wide flammable range when it is mixed with air (4 - 74 vol%) and once uncontrolled dispersion has occurred, the likelihood of local hydrogen concentration materializing in various zones of a containment building is high. The eventual outcome once an ignition source is present is deflagration or even more dangerously - an explosion. Especially in plant situations in the nuclear industry, an overpressure following an explosion could threaten the integrity of the containment and impose radioactive pollution.

In relation to nuclear safety and a hypothetical severe accident, much work has been, and is still conducted to investigate possible mitigations, with ventilation and inerting techniques being the two main paths usually taken [6, 7]. Ventilation involves providing frail areas to the confinement, preventing the pressure rise during an explosion to be confined. The hot expanding gas products and unburned fuel may escape through the weakened areas, which are designed to open once a pre-specified pressure level is reached. In nuclear plants however, requirements such as the vent size and corresponding location might be too impractical to implement for it to successfully mitigate an explosion. Inerting on the other hand works by adding a non-reactive agent such as nitrogen, carbon-dioxide or argon to diminish the flammable mixture to an adequately low level, preventing flame propagation and a possible explosion. It is however imperative that the inert gas is able to infiltrate the whole region in the enclosure to effectively suppress the flammable concentration, which may be a challenge in a building with complex geometry.

Even though it might not be capable of rendering a flammable mixture full

inert practically, steam and water mist added to a hydrogen-air mixture are two other mitigation techniques explored [8, 9]. Being ubiquitous, non-toxic, environmentally favourable and with a high heat capacity per unit mass, water has always been regarded as an ideal fire suppression agent [10]. Water mist (99% of the droplets are less than a millimetre in diameter) in particular can have a significant mitigating effect upon the burning velocity and ignition behaviour of any type of flame. With an exposed surface area depending on the droplet diameter, it reduces the rate of reaction by extracting heat from the flame, both as a liquid component and after vaporisation as a diluent [11].

Experimental studies on the interaction between hydrogen-air laminar burning velocities and water mist is currently still limited. The presence of dense water mist makes obtaining the laminar burning velocity a bit more intricate. Customarily, the burning velocity is obtained directly from the examination of flame; either by curved flames in stagnation flow, propagating spherical flames in combustion vessel, flat flames stabilized on burner or conical flames stabilized on a bunsen burner [12]. However, these methods require a clear and translucent field of vision, something a dense water mist does not apply to. It may also generate strong flame instabilities, making it harder to obtain a well-defined flame front for measure purposes.

Other methods can be employed in obtaining the laminar burning velocity that is considered less convoluted without direct observation of the flame, when more advanced means are unattainable. In a confined explosion vessel, an indirect method of obtaining a value of the flame propagation through a pressure-time history can determine the corresponding burning rate. In a constant volume vessel and assuming that the fractional pressure rise is proportional to the fractional mass burned, a relationship between the measured rate of pressure and the burning velocity can be found [13, 14].

1.2 Objectives

The objective was to develop and improve on an experimental rig whereby premixed hydrogen-air mixture was ignited. The spherically expanding flames generated were to be extracted using two methods; by a z-type schlieren imaging system and by a pressure-time history method with the latter method considered less inferior in accuracy. Both methods used in obtaining the laminar burning velocity, against each other and literature data was the ultimate deciding factor determining their validity. Finally, an introduction of water mist into hydrogen-air mixture was evaluated to see how it influenced the laminar burning velocity.

Prior to the work in this thesis, all major apparatuses needed to conduct this study was procured though the work of Halland [15] in 2015, conducting her thesis project at UoB. This included an explosion chamber, a high-speed camera, parabolic mirrors and pressure transducers.

Chapter 2

Theory

2.1 Basic concepts

This chapter describes the basic theory, with the intention of highlighting important concepts essential to the work in this thesis. Basic in the sense that the reader, already familiar with the contents or not, may reach a common fundamental perspective accordingly.

2.1.1 Combustion

In combustion processes, fuel and oxidizer (typically oxygen in air), are mixed and burned. As a phenomena, combustion is found difficult to define precisely and there exists many attempts of a formal definition. A general definition found in the literature is given below iterated by Williams [16]:

> "Combustion may be considered to be the science of exothermic chemical reactions in flows with heat and mass transfer."

Combustion is usually accompanied by the generation of heat and emission of light in the form of a flame, a self-sustaining propagation of a localized combustion zone at subsonic velocities [17]. Flame inhibits several categories based upon whether the fuel and oxidizer is mixed first and burned later, or whether combustion occurs simultaneously with the mixing, premixed and non-premixed respectively.

Tab. 2.1 illustrates examples of combustion systems that belong to each of these categories including the flow conditions. Fluid motion is conditioned

as either laminar or turbulent combustion with laminar fluid moving with low velocities lacking cross-currents or eddies [17]. Meanwhile turbulent combustion is characterized by higher velocities with the fluid moving more erratically and lateral mixing forms taking place.

Table 2.1: Combustion system ordered with respect to premixedness and flow type.

Fuel/Oxidizer	**Fluid Motion**	**Examples**
Premixed	Turbulent	Explosion
	Laminar	Bunsen flame
Non-premixed	Turbulent	Pulverized coal combustion
	Laminar	Candle

For the work of this thesis a *premixed laminar flame* is inhibited, as the fuel and oxidizer are mixed and ignited.

2.1.2 Explosions

Bang! The noise whereby a rapid increase in pressure has occurred is usually associated with an explosion. By a definition suggested by Eckhoff [18], an explosion is a exothermic process that, when occurring at constant volume, gives rise to a sudden and significant pressure rise. The energy release by the exothermic process can either be physical (e.g. bursting of a pressurized vessel), chemical (e.g. rapid combustion) or nuclear (fusion or fission) [17].

Disregarding explosives and chemically unstable substances, there are five requirements necessary for a gas explosions to occur:

1. Fuel: Combustible gas, vapour or dust
2. Oxidizer: Usually oxygen in air, but not limited to (as in the case of explosives)
3. Combustible mixture: Proper dispersion and concentrations for combustion
4. Confinement: Not a necessity for an explosion, but its impact on the pressure built up is extensive
5. Ignition source: Any heat source capable or initiating an exothermic chain reaction

2.1.3 Equivalence ratio

The equivalence ratio describes the concentration of fuel in the oxidizer and controls the combustion process as in a complete combustion there is sufficient oxidizer for all the fuel to react [17]. Defined as the the ratio of the fuel-to-oxidizer ratio to the stoichiometric fuel-to-oxidizer ratio:

$$\phi = \frac{\left(\frac{n_{fuel}}{n_{air}}\right)_{mixture}}{\left(\frac{n_{fuel}}{n_{air}}\right)_{stoichiometric}}. \tag{2.1}$$

If there is an excess of fuel, the system is fuel-rich, and if there is an excess of oxygen it is referred to as fuel-lean. Accordingly, as shown in Tab. 2.2, premixed combustion processes can be divided into three groups:

Table 2.2: Mixtures described by equivalence ratio.

Mixture	$\boldsymbol{\phi}$
Lean	< 1
Stoichiometric	1
Rich	> 1

The balanced chemical equation for a hydrogen-air mixture and a hydrogen-air-water mixture at equilibrium is given below as Eq. (2.2) and Eq. (2.3). It has been taken to account that dry air contains only about 21% oxygen and 79% nitrogen. Thus for each oxygen molecule, there are 3.762 nitrogen molecules.

$$\mathrm{H_2} + 0.5\,(\mathrm{O_2} + 3.762)\,\mathrm{N_2} \longrightarrow \mathrm{H_2O} + 0.5 \cdot 3.762\,\mathrm{N_2}. \tag{2.2}$$

$$\mathrm{H_2} + 0.5\,(\mathrm{O_2} + 3.762)\,\mathrm{N_2} + \mathrm{H_2O} \longrightarrow 2\,\mathrm{H_2O} + 0.5 \cdot 3.762\,\mathrm{N_2}. \tag{2.3}$$

In terms of volume percentage, the amount of volume fuel constituted as part of the total volume, can be used to describe the gas concentration:

$$vol\% = \frac{vol_{fuel}}{vol_{total}} \cdot 100, \tag{2.4}$$

where vol_{fuel} represents the fuel-volume and vol_{total} the total volume of the gas mixture.

The reactants and the products of the combustion can be considered as *ideal gases*, and the equation of state is applicable as follows:

$$pV = nRT, \tag{2.5}$$

where p is pressure, V is volume, n is number of moles, R is the universal gas constant and T is temperature [17].

Rearranging Eq. (2.5), the pressure can be expressed as $p = n\frac{RT}{V}$. At constant volume and temperature it can be stated that the total pressure of a gas mixture is determined by the total number of moles of gas present:

$$\frac{vol_{fuel}}{vol_{total}} = \frac{p_{fuel}}{p_{total}} = \frac{n_{fuel}}{n_{total}}. \tag{2.6}$$

2.1.4 Flammability limits

As the fuel to air ratio is either increased or decreased, there are limits to which the mixture no longer is able to propagate a flame. These two finite upper and lower flammability limits, UFL and LFL respectively, are defined by experimental determination and differ for various gasses as shown in Tab. 2.3 [19].

Table 2.3: Flammability limits for various gasses.

Gas	**Flammability limit vol%**	**Flammability limit vol%**
	Lower	Upper
Hydrogen	4.0	75.0
Methane	5.0	15.0
Propane	2.1	9.5
Acetylene	2.5	100.0

2.1.5 Thermodynamic properties

Heat capacity describes the amount of heat required to change the temperature of a substance. For an ideal gas, Mayer's relation between the specific heat at constant pressure and the specific heat at constant volume is derived as:

$$C_p - C_v = R_s, \tag{2.7}$$

denoting C_p as the specific heat capacity at constant pressure, C_v as the specific heat capacity at constant volume and R_s the specific gas constant [17]. C_p can be expressed empirically allowing adjustments as the temperature changes. Usually, the molar heat capacities are expressed as a five-term polynomial of fourth order. Used in FLACS, Arntzen [20] simplified the polynomials into a second degree polynomial, at constant pressure becoming:

$$C_{p,i} = a_i + b_i T, \tag{2.8}$$

citing a and b as specific heat capacity coefficients of temperature and are unique for each gas, i. Tab. 2.4 contains values for a and b for hydrogen, nitrogen, oxygen and water.

Table 2.4: Specific heat capacity coefficients for various gases.

Gas	a_i	b_i
H_2	13600	1.719
N_2	950	0.112
O_2	1036	0.118
H_2O(l)	4000	0.550

A ratio describing the heat capacity at constant pressure to heat capacity at constant volume is denoted by:

$$\gamma = \frac{C_p}{C_v}. \tag{2.9}$$

2.2 Laminar burning velocities

The propagation rate, commonly called the burning velocity for any fuel is an important parameter tool, both as an input parameter and also for validation of combustion kinetics simulations. A one-dimensional combustion model can be derived for the laminar burning velocity describing the unburned gas-air mixtures being absorbed by the combustion reaction. Making measurements on real flames and transforming them, required one-dimensional values not present in nature can be obtained. Idealized adiabatically with no heat loss, no buoyancy and no interference by the wall, a planar laminar combustion at constant pressure has been illustrated by Eckhoff [18], see Fig. 2.1. If the gas mixture is ignited in the open end of the tube (Fig. 2.1a), the

combustion products will expand freely into the ambient atmosphere, and the observed flame speed S_f will be the same as the laminar burning velocity S_u. The distinction between the observed absolute flame speed and the laminar burning velocity is of vital importance as the latter is only defined relative to a fixed reference frame. Shown in Fig. 2.1b, ignition in the closed end of the tube will cause the expansion of the combustion produced to occur in the same direction as that of the flame propagation, with the burned gas generated behind being stationary. Therefore the observed flame speed S_f, in relation to the tube wall, will be the sum of S_u and the unburned gas flow velocity S_g.

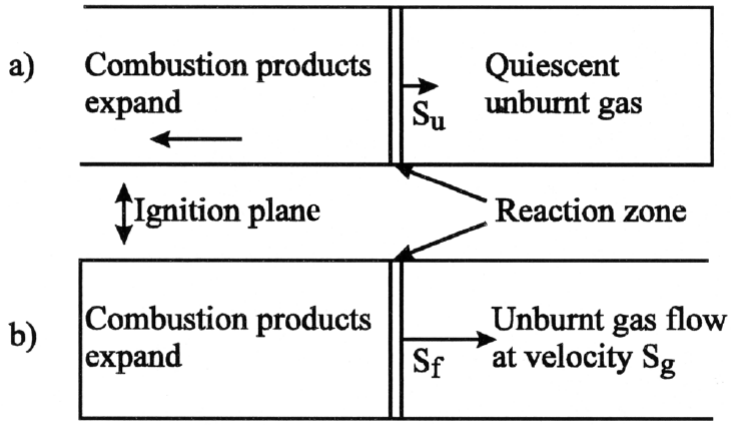

Figure 2.1: One-dimensional combustion model with premixed fuel gas-air burning at constant pressure with a plane, laminar flame in a tube [18].

Similarly, in spherically expanding flame as shown in Fig. 2.2, the absolute flame speed S_f can be observed directly measuring the velocity from the center as the flame expands, i.e change in the radius with respect to time:

$$S_f = \frac{dr_f}{dt}, \tag{2.10}$$

where dr_f is the change in radius, and dt change in time.

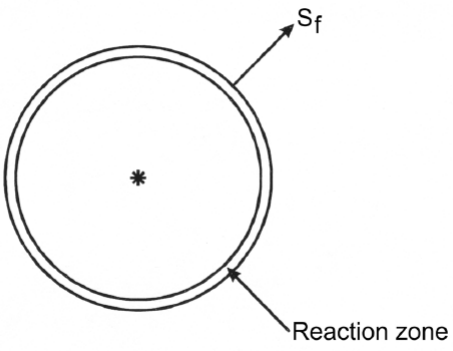

Figure 2.2: Ideal laminar spherical burning and expansion of a premixed gas/air mixture, after ignition at midpoint [18].

It can be further compared to the linear one-dimensional case, whereby ignition occurs in the closed end, that the spherically expanding flame is a combination of the burning velocity and the unburned gas flow velocity. Assuming a very thin flame and negligible buoyancy, the unburned gas mixture will always be pushed in the direction of the propagation. The relationship between the absolute flame speed S_f and the laminar burning velocity S_u can be shown as:

$$S_f = \frac{dr_f}{dt} = \frac{\rho_u}{\rho_b} \cdot S_u = E \cdot S_u, \tag{2.11}$$

defining E as the expansion ratio with ρ_u and ρ_b being the gas density of the reaction, unburned and burned respectively. [18].

2.3 Flame Stretch

A flame front propagating in a non-uniform flow is subject to strain and curvature effects, and these changes in notion are measured by flame stretch. Defined by Poinsot and Veynante [21], flame stretch is a fractional rate of change of a flame surface element and can be expressed as:

$$\alpha = \frac{1}{A}\frac{dA}{dt}, \tag{2.12}$$

where A is flame surface area. Writing the stretch rate in terms of the radius of the sphere gives:

$$\alpha = \frac{1}{A}\frac{dA}{dt} = \frac{2}{r_f}\frac{dr_f}{dt}, \tag{2.13}$$

and finally expressed as a function of the absolute flame speed by combining with Eq. (2.10):

$$\alpha = \frac{2}{r_f}S_f, \tag{2.14}$$

presenting the total flame stretch as the sum of stretch caused by the flow non-uniformity and the stretch caused by the curvature found locally in the reaction front.

2.4 Estimating burning velocities

Flame speed whereby all speeds can be unambiguously defined and measured is rarely the case, as flames are subject to stretch effects of varying degree due to thermo-diffusive and hydrodynamic nature within and ahead of the flame. This makes it more difficult to evaluate both numerically and experimentally.

At an early stage of a spherical flame propagation, the flame stretch effects are considerable and the pressure rise negligible. Later however, the pressure rise rate increases greatly and the stretch becomes negligible. These two behaviours describes the two different methodologies in extracting the burning velocity, with the former being the constant-pressure method, and the latter the constant-volume method.

2.4.1 Constant-Pressure Method (CPM)

The linear extrapolation methodology

Studies reiterated by Poisont and Veynante [21] suggests that in the limit of small strain and curvature terms, stretch (α) is the only parameter controlling

the flame structure and therefore, the displacement and consumption speeds through a linear relationship:

$$S_{f_s} = S_{f_u} - L \cdot \alpha, \tag{2.15}$$

defining L as the Markstein length, S_{f_s} as the flame speed and S_{f_u} the value of the unstretched flame speed. The Markstein length describes the linear relationship between the stretch of the flame, either strain or curvature, and the flame speed. In other words, it is a measure of of how much the stretch of the flame is influenced by the flame speed - the higher the Markstein length, the larger the effect of stretch of the flame.

The non-linear extrapolation methodology

Through the work of Kelley and Law [22], a consideration of non-linearity between the flame speed and the flame stretch rate is determined. Restricting their analysis to "flames that are adiabatic and propagate in a quasi-steady manner", it is expressed as:

$$\left(\frac{S_{f_s}}{S_{f_u}}\right)^2 ln\left(\frac{S_{f_s}}{S_{f_u}}\right)^2 = -2\frac{L \cdot \alpha}{S_{f_u}}. \tag{2.16}$$

The non-linearity was confronted in the flame response as a consequence of the small diffusivity of heavier fuels, casting considerable uncertainty on the feasibility and accuracy of the conventional method of linear extrapolation.

Both the linear and non-linear extrapolation method will be utilised to optimize estimation of the laminar burning velocity using the constant-pressure method.

2.4.2 Constant-Volume Method (CVM)

The dynamic pressure-time history in a closed vessel explosion can be used to obtain the laminar burning velocity through different relations. The validity of the pressure-time history approach is according to Omari and Tartakovsky [23] based on the following assumptions in addition to ideal gas behaviour and uniform pressure distribution:

- The confinement acts against the expanding burned gas and hence, (S_f) is not equal to the propagating flame outwards, but a combination of both the unburned gas flow velocity and laminar burning velocity
- The confinement implies a pressure rise which is followed by a temperature rise due to compression. Thus, the burned and unburned gas temperature, as well as its density, continuously increases during flame propagation.
- In the analytical confined flame model, the flame stretch is neglected. This is justified by realizing that during the pressure rise period, r_f is large and the flame front speed (dr_f/dt) strongly reduces, thus contributing to a continuously decreasing stretch rate, α.

The first expression consisting of both the dynamic pressure rise and optical accessed flame radius is known as the Fiock and Marvin expression [24] and is given as:

$$S_u = \frac{dr_f}{dt} - \frac{R_v^2 - r_f^3}{3\gamma_u r_f^2} \frac{1}{p} \frac{dp}{dt}, \tag{2.17}$$

where p is the dynamic pressure; γ_u is the specific heat ratio of the unburned gas; R_v is the radius of the vessel. The first term represents the absolute flame speed, S_f, and the second term representing the unburned gas flow velocity through the pressure rise inside the vessel, S_g.

A second and more widely used expression, only utilising the dynamic pressure rise is possible. To do so, the mass fraction x related to the pressure rise is found corresponding to the radius of the flame as:

$$\frac{r_f}{R_v} = \left[1 - \left(\frac{p}{p_i}\right)^{-1/\gamma_u} (1 - x(p))\right]^{1/3}. \tag{2.18}$$

When using the confined flame model equation and considering x to be obtainable from pressure monitoring i.e. $x = x(p)$, the laminar burning velocity at elevated temperature and pressure, S_u is extracted from the pressure rise using the following equation:

$$S_u = \frac{R_v}{3} \frac{dx}{dp} \frac{dp}{dt} \left(\frac{p}{p_i}\right)^{-1/\gamma_u} \left[1 - \left(\frac{p}{p_i}\right)^{-1/\gamma_u} (1 - x(p))\right]^{-2/3}, \tag{2.19}$$

The derivation itself is from O'Donovan and Rallis [25] and is described in detail in their work.

Relating the burned mass fraction x to the pressure rise during a constant volume, taking into account the temperature rise in both the burned gas and the unburned gas zone, the analytical $x - p$ relation proposed by Luijten et al. [26] considers energy conservation in the whole combustion vessel and is as follows:

$$x = \frac{p - p_i \cdot f(p)}{p_{max} - p_i \cdot f(p)}, \tag{2.20}$$

with $f(p)$ being:

$$f(p) = \left(\frac{\gamma_b - 1}{\gamma_u - 1}\right) + \left(\frac{\gamma_u - \gamma_b}{\gamma_u - 1}\right)\left(\frac{p}{p_i}\right)^{\frac{\gamma_u - 1}{\gamma_u}}. \tag{2.21}$$

p_{max} is the final pressure defining the final maximum pressure obtained when all of the gas is burned. Differentiating is straightforward, yielding:

$$\frac{dx}{dp} = \frac{1 - p_i f'(p)}{p_{max} - p_i f(p)} + \frac{p_i f'(p)[p - p_i f(p)]}{[p_{max} - p_i f(p)]^2}, \tag{2.22}$$

where,

$$p_i f'(p) = \left(\frac{\gamma_u - \gamma_b}{\gamma_u}\right)\left(\frac{p}{p_i}\right)^{-1/\gamma_u}. \tag{2.23}$$

Both Eq. (2.20) and Eq. (2.22) are inserted into the the differential Eq. (2.19), and evaluated computationally using MATLAB. The end result is not written explicitly as it is not considered necessary.

Once S_u is extracted, the value for S_{u_0}, defined at reference conditions of pressure as the one-dimensional laminar burning velocity, can be established. The following equation is by Omari and Tartakovsky [23]:

$$\frac{Su}{S_{u_0}} = \left(\frac{T_u}{T_i}\right)^a \left(\frac{p}{p_i}\right)^b, \tag{2.24}$$

For a constant-volume adiabatic combustion, the unburned gas temperature rises due to isentropic compression and hence, Eq. (2.24) can be simplified into:

$$\frac{Su}{S_{u_0}} = \left(\frac{p}{p_i}\right)^{\alpha}, \tag{2.25}$$

where $\alpha = a((\gamma_u - 1)/\gamma_u) + b$. Exponents a and b are weak functions of the equivalence ratios, and these values in addition to S_{u_0} are fitted accordingly for each mixture.

2.5 Schlieren imaging technique

Air as we see it is experienced transparent with it propagating homogeneously through around us. Looking at other phases in likewise transparent form such as water and ice, one might see a reflection of the image around and even more importantly, a refraction of the transparent media showing the background. Air may be without reflection, but it does have very weak refractive indices and although invisible to the eye, can be apparent with the schlieren imaging technique.

The basic concept of a schlieren imaging system, is to translate phase fluctuations into a visual optical image. In aerodynamics, flow visualization can be conducted in which changes in the index of refraction due to variation of the flow density, pressure or temperature can be measured. To apply quantitative analysis to schlieren optics systems, the physics behind are outlined with guidance of the work of Settles, Mazumdar and Lien et al. [27–29].

2.5.1 Light propagation

The refractive index, as light interacts with matter is given as

$$n = c/v. \tag{2.26}$$

This indicates change through a transparent medium, with c being the universal speed of light in a vacuum, $3 \cdot 10^8$ m/s, and v the light speed in the

medium. In the case of air and other gases, there is a simple relation between the refraction index and the gas density (ρ) showing:

$$n - 1 = k\rho, \tag{2.27}$$

that puts the density in relation to n and k, the Gladstone-Dale coefficient, which is specific for every gas and its conditions, and varies between 0.1 and 1.5 cm^3/g.

A simple interpretation of schlieren light refraction is best imagined in the light of a x, y, z-coordinate system. In a simple 2D-case, a planar light wave along the z-axis becomes displaced after propagating through an area of optical inhomogeneities in proportion to the refractive index. As shown in Fig. 2.3, light initially vertical becomes bent over a differential distance in $\Delta z/\Delta t$.

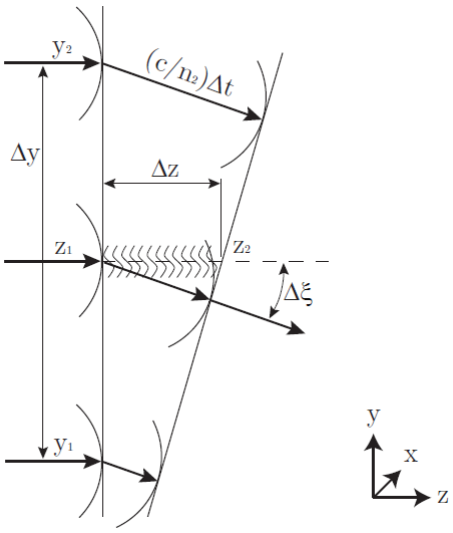

Figure 2.3: Diagram of light rays entering a new material and being refracted in proportion to a refractive-index gradient [28].

With a differential angle $\Delta\xi$, the refractive index from Eq. (2.26) can be rewritten to give an en expression of the angle:

$$\Delta\xi = \frac{c/n_2 - c/n_1}{\Delta y}\Delta t. \tag{2.28}$$

The differential time Δt can be expressed by the differential distance Δz and the local velocity $v = c/n$, and by simplifying leads to:

$$\Delta\xi = \frac{n}{n_1 n_2}\frac{(n_1 - n_2)}{\Delta y}\Delta z. \tag{2.29}$$

The term $^{n}/_{n_1 n_2}$ can be simplified to $1/n$ in the limit as Δy approaches zero. Letting all finite differences approach zero yields:

$$\frac{d\xi}{dz} = \frac{1}{n}\frac{dn}{dy}. \tag{2.30}$$

Implementing the equation above for a more general case where other refractive index gradients may occur, it is possible to postulate that the angle ξ is equal to dy/dz. Enforcing this and turning from total derivatives to partial derivatives to account for the general case, we may obtain for the ray curvature in the y-direction:

$$\frac{\partial^2 y}{\partial z^2} = \frac{1}{n}\frac{\partial n}{\partial y}. \tag{2.31}$$

In similar terms, the ray curvature in the x-direction may be given:

$$\frac{\partial^2 x}{\partial z^2} = \frac{1}{n}\frac{\partial n}{\partial x}. \tag{2.32}$$

Eq. (2.31) and (2.32) both indicate light defections bending towards areas of higher refractive index. That is, the larger the refractive index gradient is, the larger the angle of refraction.

2.5.2 The z-type two mirror schlieren system

When setting up a standard schlieren system there are two major categories for collimating and focusing the light: convex lenses and parabolic mirrors [30]. The two groups differ very little optically, although using mirrors has become preferred as the most used approach as quality of parabolic mirrors has improved substantially [31]. Furthermore, for larger flow visualisation, mirror set-ups are favourable, and will be the subject of this section.

Using two identical parabolic mirrors on each side of the test area, in addition to a light source, a knife-edge and a capturing device, a z-type schlieren system may be achieved. Setting up the components in a single zigzag-line that suggests the letter z, its name is inspired by the distinguishable set-up. As seen with a simple sketch in Fig. 2.4, the light source is placed with a certain angle θ sending a collimated beam of light to the first parabolic field mirror. A parallel beam between the mirrors through the test area reaches the second mirror. The second mirror with the same angle θ on the opposite side of the centerline is pointed towards a knife-edge.

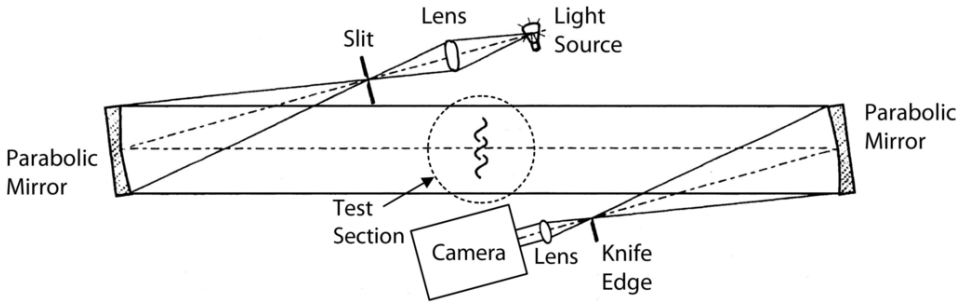

Figure 2.4: Z-type schlieren arrangement [27].

The task of the knife-edge, positioned at the focal point of the mirror, is to block a portion of the incoming light. This allows the unblocked light to show gradients in the light intensity depending on the refractive index. In the test area, higher density gradients will be visible by brightened and/or darkened intensity in the pictures compared to the background. An example of this is shown in Fig. 2.5, as the density contrast in the explosion products propagation.

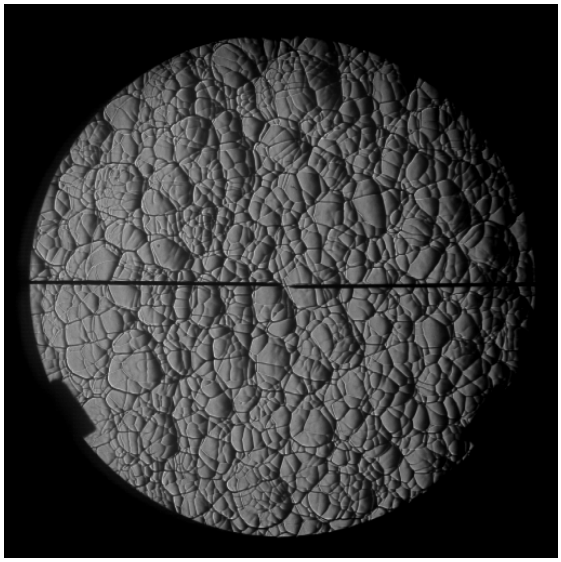

Figure 2.5: Schlieren image showing density gradients in the test area after a hydrogen-air explosion.

Chapter 3

Previous work

3.1 Laminar burning velocities of hydrogen-air mixtures

Experimentally, quantitative investigation and determination of gaseous mixture combustions have been developed and upgraded since the first recorded estimation of a burning rate of a methane-air flame published in 1815 by Sir Humphrey Davy [32]. In the period up until today, the definition of burning velocity has evolved as the experimental work has progressed. Taking into account of the effect of stretch on propagating flames, a shift in the techniques used ensued. Stabilized (stationary) measurement technique, such as flat flame burners and counter double flame were exchanged for a spherical expanding flame technique. It was after a critical review done by Andrews and Bradly [33] which considered it to be the best method for measuring propagating flame velocity, although in present times it is still an ongoing discussion. A research paper by Gelfand et al. [34] collected data illustrating the trend of different methods and corresponding results of hydrogen-air mixture, presented in Tab. 3.1. Even when the method applied was alike, discrepancies still occurred in S_u^{st} and S_u^{max}, implying that there are still uncertainties present due to radiation, stretch effects, confinement and preferential mass diffusion effects [23].

Something in common with the spherical expanding flame techniques is the complexity in data processing and needed requirements in equipment such as a high-speed camera and parabolic mirrors. Therefore, a labour and cost-effective burning velocity measuring method was convenient using a

Table 3.1: Data by various authors showing the hydrogen-air premixed laminar burning velocity measured at stoichiometry, S_u^{st}, and maximum, S_u^{max}, using different methods [34].

Author	Year	Method	% H_2	S_u^{st}	S_u^{max}
Michelson	1889	Bunsen burner	15.3–74.6	217	281
Jahm	1934	Bunsen burner	30–75	187	267
Bartholome	1949	Nozzle burner	40–51.2	–	320
Kozachenko	1954	Fantail burner	20–70	233	287
Manton and Milliken	1956	Spherical flame	30–70	232	300
Fine	1956	Bunsen burner	28–62	193	304
Heimel	1956	Bunsen burner	28–57	206	297
Grummer	1959	Spherical flame	48–67.1	–	–
Senior	1961	Bunsen burner	17.4–33	200	–
Gunther and Janisch	1972	Nozzle burner	15–70	282	355
Andrews and Bradley	1973	Two sources method	10–70	–	336
Liu and MacFarlane	1983	Nozzle burner	20.6–64	–	356
Takahashi	1983	Nozzle burner	29.6–64	–	308
Wu and Law	1984	Nozzle burner	22.7–70	–	332
Wu and Law	1984	Nozzle burner	29.6–62.7	–	308
Iijima and Takeno	1986	Spherical flame	17.4–62.7	238	298
Dowdy, Smith, Taylor	1990	Spherical flame	9–68	213	286
Egolfopoulos, Law	1990	Counter-flow	9.7–38.6	209	
Koroll, Kumar, Bowles	1993	Two sources method	8–70	250	346
Koroll, Kumar, Bowles	1993	Nozzle burner	30–70	250	330
Vegelopopoulos and co-authors	1995	Counter-flow	9.5–18.8	–	–
Faeth and co-authors	1998	Spherical flame	15.9–62.7	210	247
Law and co-authors	2000	Spherical flame	15.9–627	190	282
Langmuir and co-authors	2003	Spherical flame	10–60	209	282
Huang and co-authors	2006	Spherical flame	20–38.7	224	–

confined method based on the pressure-time history approach, with perceivable decreased accuracy [35]. A study done by Dahoe [14], used a 169 ml vessel and compared laminar burning velocities obtained with other laminar burning velocities which concluded in unison results. Illustrated in Fig. 3.1, it was seen that data obtained using CVM (straight line) were seen to fall within the scatter of data obtained by more advanced methods fully taking into account the influence of flame stretch.

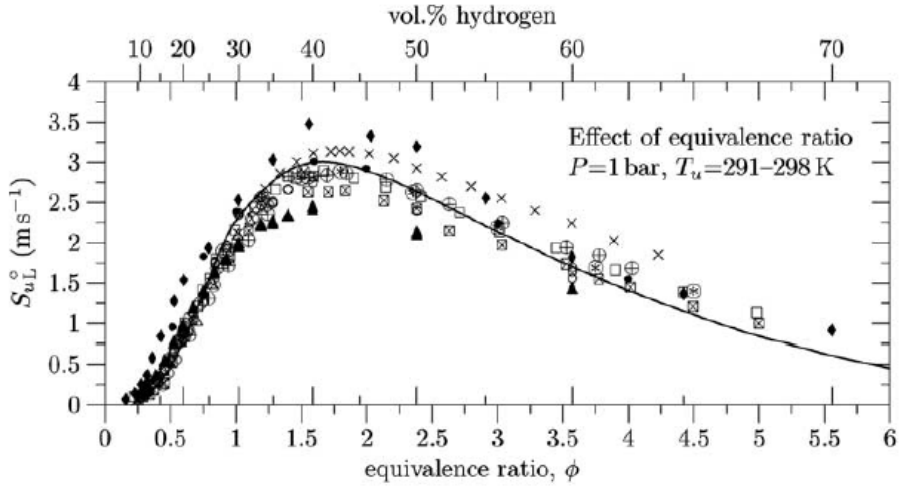

Figure 3.1: The comparison of laminar flame velocities of hydrogen-air mixtures measured by various techniques [14].

3.2 Laminar burning velocities of hydrogen-air mixtures exposed to water mist

Dividing water into fine droplets gives it new properties and capabilities, which has constantly been explored since the mid 1950s [36]. Measuring the effectiveness of an inhibiting agent such as water mist can be done by examining the laminar burning velocity as an indicator. It indicates the relative effectiveness of suppressants in isolation from other factors affecting burning velocity, also noting that the reduction in burning velocity is not simply proportional to the change in heat capacity of the mixtures [37].

Experiments on the behaviour of premixed hydrogen-air mixtures exposed to water mist has been conducted by Cheikhravat et al. [38] using a 56 litre spherical vessel at atmospheric conditions. Visualization of the flame by

schlieren imaging technique made it possible to investigate the interaction of a flame with water droplets, as shown in Fig. 3.2. Focusing on the water droplets' characteristics, it was found that the droplet effect on the flame depends strongly on the droplet diameter. To quench the flame efficiently, the droplet must be totally evaporated during the residence time in the flame front thickness. A Sauter Mean Diameter (SMD) $\approx 5\ \mu m$ reduced the burning velocity over a wide range of equivalence ratios ϕ = 0.6-2.9, and also slightly mitigating the final maximum pressure p_{max}. Relatively large droplets (SMD = 200-250 μm) was also investigated showing mitigating effect to the evolution of the combustion.

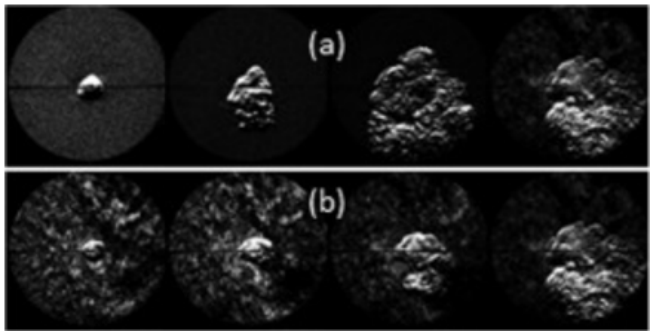

Figure 3.2: Ignition and propagation of hydrogen-air-mist flame fed through a nozzle initially at 305 K and 1 bar without(a) and with(b) water mist [38].

van Wingerden et al. [39] exhibited laboratory-scale tests done with methane-air mixtures proving water droplets maximum effectiveness in mitigation laminar burning velocities in the order of 10 µm. These droplets had then the capability of evaporating fully in a laminar flame, established using Fig. 3.3. To achieve full evaporation, it was approximated a flame thickness of 1 mm and a residence time of the droplet in the flame of 2 ms. For higher relative velocities, such as in a hydrogen-air combustion, the evaporation time would decrease as well as the residence time. Therefore it could also be concluded that at higher relative velocities, only droplets smaller than 10 µm would fully evaporate.

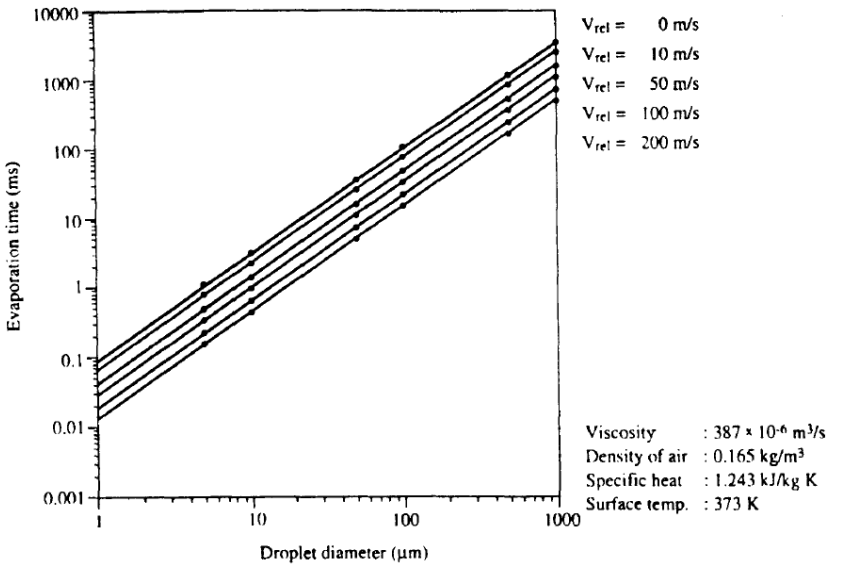

Figure 3.3: Evaporation time as a function of droplet diameter for various relative hot gas flow speeds around the droplet [39].

Studies by Holborn et al. [40–42], both experimentally and by modelling, showcased that fine water mist (5-6 µm) reduced the estimated burning velocity for hydrogen-air mixtures significantly. Experimentally using the pressure-time history method was applied to a large number of test data sets. It confirmed that high concentration water mist fogs (0.2-0.3 kg/m^3) reduced the laminar burning velocity for both lean and rich hydrogen-air mixtures. It was also deducted that the peak overpressure for lower concentrations of hydrogen-air mixtures up to 20 vol% ($\phi < 0.6$) could be significantly reduced, but would require very high fog densities when the highest rate of pressure rise is present near stoichiometric mixtures.

Not all instances of water mist fog introduction result in lower laminar burning velocities. Geometry dependencies are also to be accounted for, when water spray is introduced into large volumes. Investigation into turbulence generation by water-spray systems has been very limited, especially in a hydrogen-air atmosphere prior to ignition. van Wingerden and Wilkins [43] addressed the influence of turbulence generated by these systems on the course of gas explosion. Quantitatively, they found a burning rate increase factor from 1.5 to 2 for propane and 1.4 to 2.3 for methane, with the main source of turbulence relating to the bulk flow of water mist into the vessel. The droplet size or other parameters related to the droplet velocity had minor influence.

Chapter 4

Experimental set-up and procedure

This section describes the experimental equipment, set-up and general procedure. Essential equipment such as the high-speed camera and explosion chamber were already available in the lab for usage. Other equipment such as the data acquisition module and water cylinder were borrowed from Gexcon. The set-up and general procedure described were the established final arrangement and approach.

4.1 Experimental rig

4.1.1 Explosion chamber

The explosion chamber used for the work described in this thesis was a chamber previously used by Halland [15] and built by Skjold [44], where a detailed overview of the chamber can be found. For optical access to the explosion, there were two circular windows mounted on opposite sides of the sides for free sight through the chamber. Other holes were installed for inlet and outlet of gases, and for pressure sensors. For this work, an additional hole at the bottom of the chamber was made for inlet of water mist and its dispersion. Before the aforementioned hole was made, the total volume measured by water filling proved to be 20 235 cm^3 with the dimensions being 27.3 cm x 27.3 cm x 26.7 cm. A test carried out certified that the chamber could cope with pressures up to 20 barg. A general set-up of the explosion

chamber and the equipment connected to it is presented in Fig. 4.1.

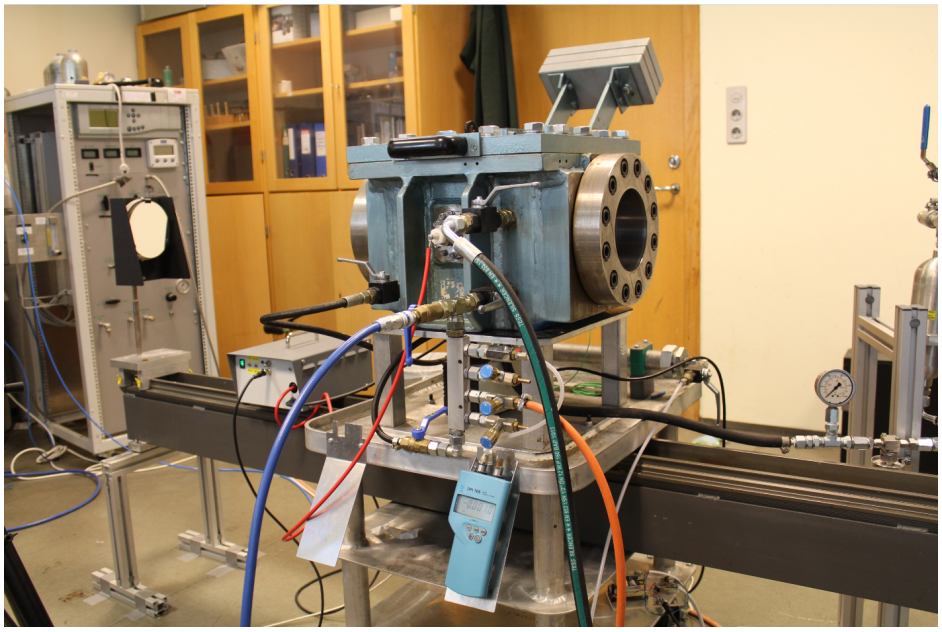

Figure 4.1: 20-litre cubical explosion chamber.

4.1.2 Windows

The windows mounted to the chamber consisted of two disks of natural fused quartz glasses, with a thickness of 51 mm and a diameter of 144 mm. Being of high quality, the glasses provided an unblemished background for light to propagate through. Irregularities inevitably present in or on the surface of the low-quality glass, be it small cracks, scratches or fragments, may cause a minor deflection on the light and sabotage the quality of the schlieren images.

4.1.3 Piezoelectric pressure sensor

A quartz pressure sensor type Kistler 7031 with a pressure range up from 0-250 bar was utilized for measuring the dynamic pressure rise throughout the explosion with a frequency range up until 80 kHz. The built-in accelerometer compensates interference signals produced by shock or vibration in the direction of the sensor axis acting through the diaphragm on the quartz crystal measuring element. The signal is then transformed from pressure into an electric charge.

The pressure sensor was mounted in the explosion chamber wall with a Kistler 7501 mounting adapter, sealing off and impeding external liquids from entering into the connector and corrupting the sensors electrical isolation. Finally a Kistler 7401 BNC-mounting nipple was connected to the adapter attaching the pressure sensor to the charge meter, a Kistler 5015. The sensor, adapter and nipple is presented in Fig. 4.2. The charge meter connects to the computer displaying instantaneous, peak and average values converting the electric charge back to pressure values. The cable to remotely control the charge amplifier was not available in the laboratory at the time. Therefore, activating the charge amplifier had to be done manually just before starting the triggering sequence to reduce the certain drifting of the pressure sensor.

Figure 4.2: From left to right - Piezoelectric pressure sensor (Kistler 7031); Mounting adapter (Kistler 7501); BNC-mounting nipple (Kistler 7401).

4.1.4 Ignition system

A capacitive spark generated in the gap between two horizontal electrodes centred in the chamber ignited the flammable mixture in the chamber. The electrodes were connected to a spark generator made and modified by Werner Olsen, a senior engineer in electronics employed at UoB. The energy released by the spark generator varies depending on the type of electrodes used and the spark-gap length. In this work, sharpened wolfram electrodes were used with a thickness of 2 mm. The spark gap was adjustable and was usually fixed at $\approx$ 2 mm, giving the distance for a successive energy release.

Energy stored in a capacitive spark can be calculated by:

$$E = \frac{1}{2}CU^2, \tag{4.1}$$

where C is the capacitance and U is the voltage.

The capacitor used had a voltage of 362 V and a capacitance of 0.2 µF, and by using Eq. (4.1) gave an energy of 13.1 mJ. Energy losses in radiation, to the electrodes, because of skin effect resistance reduces the theoretical calculated energy by 60-90%, concluded in a study done by Randeberg et al [45]. Werner Olsen, one of the authors, with additional regards to the spark-gap approximated an energy loss of up to 75%, therefore giving a more correct value for the effective energy released to be 3.27 mJ. This value was significantly higher than the minimum ignition energy measured by Ono et al. [46] to be only 0.019 mJ. This was to ensure ignition independent of mixtures, spark gap and existence of different phases when water mist is present. A more accurate method of measuring the actual energy released with a oscilloscope was attempted, but was later sidelined due to complications in signal observations.

4.1.5 Vacuum and gas delivery system

A N86 KTP Laboport vacuum pump was used to evacuate the contents of the explosion chamber between each test at a nominal flow rate of 5.5 L/min. The mixture preparation was performed by following Dalton's law of partial pressures, stating that in a mixture of non-reacting gas, the total pressure exerted is the sum of the partial pressures of the individual gasses. A real-time value of the internal chamber pressure was given by a Druck DPI 705 IS (-1 to 1 bar range) hand-held manometer with a 0.1 mbar gauge readout resolution with a full scale accuracy of 0.1%. Hydrogen of 99.9999 % purity and compressed air was introduced into the chamber by means of needle valve control, allowing for fine adjustment of the internal partial pressures.

4.2 The schlieren optical system

4.2.1 Field mirrors

Two spherical field mirrors were used as part of the z-type alignment. Both mirrors were identical with 150 mm in diameter(D) and with focal length(f) of 1500 mm. The focal length is a measure of light convergence. Any mirror can be characterized based on their diameter and focal length by the following equation describing the f/number:

$$f/_{number} = \frac{f}{D}. \tag{4.2}$$

The f/number for the mirrors used in this work describing the speed and clarity of the optical system was f/10. The lower the f/number, the wider, or bigger the aperture. Both mirrors were attached to metal sticks mounted to a metal beam. The sticks had lines engraved for easy adjustment and integrating the same height.

4.2.2 Light source, lens and slit

The light source was a single Light-Emitting Diode (LED) lamp with separated battery holder and charger, demounted from a rechargeable head torch model MF-H05. It has two power modes - high power with a capacity of 350 lumen and low power with a capacity of 180 lumen, with the former mode being used. The use of a LED lamp instead of a light source directly connected to a wall socket is related to the current delivered. Power sockets provide an alternate current, interchanging its direction with a 50 Hz frequency, which is little favourable when filming in high-speed. A LED-lamp with batteries however delivers a direct current, flowing only in one direction thereby without any fluctuation in the light on view.

The divergent beam from the LED-lamp was fixated on a condenser lens with aim to render the beam converging it towards a circular slit. The lens has a diameter of 90 mm with a focal length of 150 mm. An iris diaphragm acted as a slit with an opening at its center, with an adjustable opening in the diaphragm thus varying the amount of light let through the slit opening. It was placed at the focal point of the condenser lens and functioned as the point light source towards the first mirror. The lamp mounted focused on

the condenser lens, with the converging beam focused on the slit acting as the point light source is presented in Fig. 4.3.

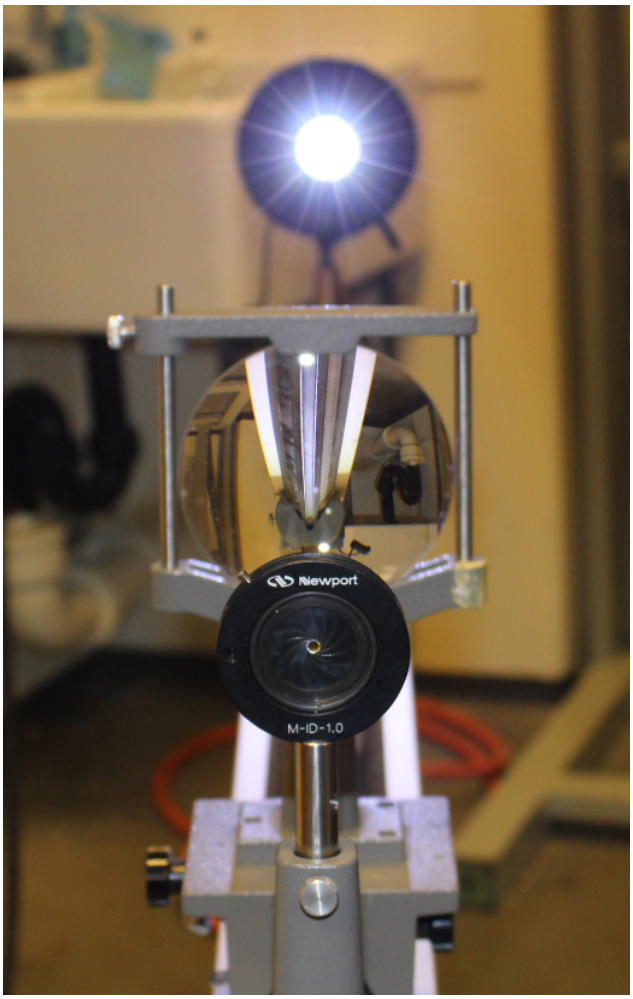

Figure 4.3: Light, lens and slit aligned accordingly.

4.2.3 Knife-edge

A knife-edge was used as a cut-off of the refracted light towards the camera. The knife-edge was effectively a utility knife, mounted vertically on a tripod. Considering the positioning tweaks a knife-edge required, a tripod was favourable for its adjustability. Positioning of the knife-edge plays a significant role in the quality of the schlieren image recorded. Demonstrated in Fig. 4.4, a correctly positioned knife-edge will uniformly darken the image.

This is opposed to if the knife edge is too close or too far away from the second mirror.

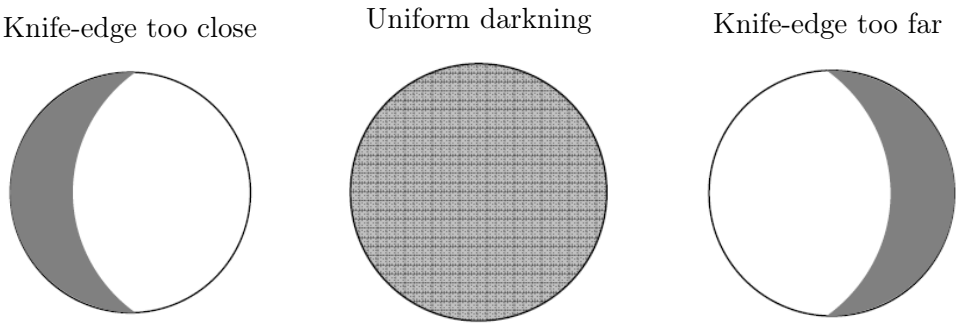

Figure 4.4: Illustration of the effect of the knife-edge movement on the schlieren image for a vertical knife edge cutting parts of the light beam.

4.2.4 High-speed camera

The high-speed camera used in the schlieren system was a Photron Fastcam SA4 RV, and could produce 3 600 frames per second (fps) with 1024x1024 pixel resolution, and operate frame rates up to 500 000 fps at a much reduced resolution. For the experiments conducted in this work, a frame rate of 20 000 fps with a corresponding resolution of 512x325 pixels was chosen as a middle ground between resolution and frame rate. The images were initially stored in the camera unit and then transferred to a computer before being processed.

The high-speed camera control, image and video editing and download software, Photron FASTCAM Viewer (PFV), was used. It enabled easy set up of the camera as well as adjustments of the frame rate, resolution and shutter-speed. Mounted to the high-speed camera was a Tamron macro lens with a focus ring clutch-type manual focusing and had a focal length from 70-200 mm with a fast F2.8 constant maximum aperture. For zooming purposes, a lens of this nature was essential in being able to magnify into the schlieren image and viewing details such as ignition spark and the instabilities in the spherically expanding flame.

4.3 Data acquisition and triggering system

For a systematic and proper routine during the test sequence, a data acquisition module, NI USB-6259, from National Instruments was utilized, see Fig. 4.5. It provided analog and digital triggering, and was optimized for superior accuracy at fast sampling rates. A corresponding program developed in LabVIEW by Gexcon was used to trigger all the required components using BNC-cables with a 5 V pulse; camera, charge amplifier, spark generator and solenoid valve.

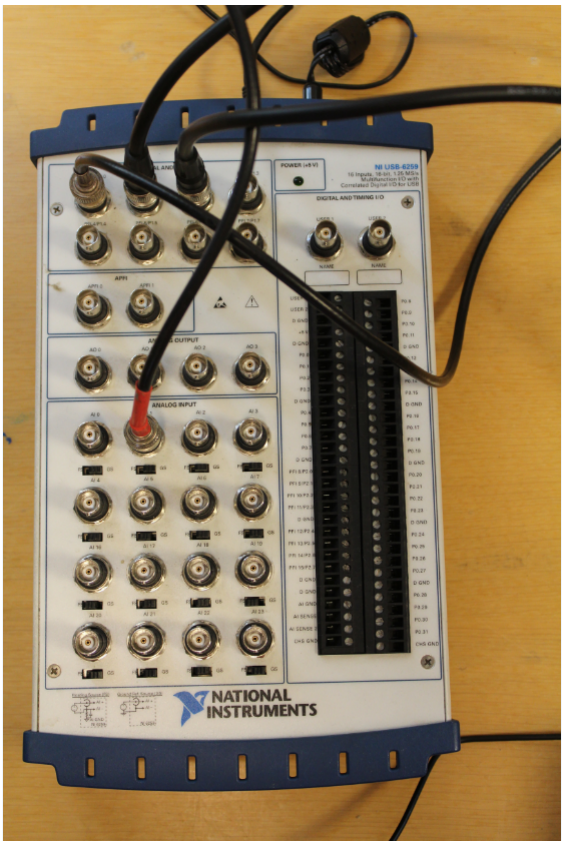

Figure 4.5: Data acquisition module, NI USB-6259, used for equipment-triggering and acquisition of amplified pressure signals in pressure measurements.

The charge amplifier was utilized by the data acquisition module to designate the duration of the measure time of the pressure, and the measure frequency. In this work, a frequency of 50 000 Hz was chosen to ensure sufficient pressure data points, obtaining $\approx$ 300 points from ignition to maximum pressure value.

4.4 Water mist implementation

4.4.1 Nozzle

The spray characteristics were delivered by a BETE 1/8" male pipe size PJ6 misting nozzle. Utilizing the kinetic energy of the liquid to break it up into droplets, it distributes a virtually homogeneous mist with a coverage at approximately 203 mm and with a spray height of around 103 mm. A nozzle producing a certain flow rate at a given pressure has a unique K-factor, a nominal discharge coefficient relating the flow rate and pressure. Nozzles with low K-factor require higher pressures than that of nozzles with higher K-factor values, to achieve the same flow rate. Knowing the pressure at the nozzle (p_{nozzle}) with a manometer mounted right before injection, the flow rate can be found as:

$$\text{Flow rate}(^{l}/_{min}) = K\sqrt{p_{nozzle}}. \tag{4.3}$$

BETE PJ6 nozzle applied has a K-factor of 0.0137, and required a p_{nozzle} = 10-70 bar to achieve 0.043 to 0.114 litre/min, operated with a flow angle of 90°. The nozzle was mounted on the bottom of the chamber, out of practical reasons and to counteract the gravitational forces working on the water mist droplets. The nozzle was installed throughout all the tests, with and without water mist, so to keep the configuration inside of the chamber consistent.

4.4.2 Water delivery system

A double ended Swagelok^{TM} 1 litre stainless steel cylinder was mounted to a stand and connected to an air-pressurised tank. The continuously compressed air supply ensured constant water pressure during water application. The cylinder had a pressure rating of up until 124 barg, far above the scope of the work in this thesis. For the water mists generation, ordinary tap water filled the cylinder, and compressed air was delivered up to 50 bar of pressure. An image of the set-up is shown in Fig. 4.6. A high-pressure pneumatically actuated bellows-sealed valve from Swagelok^{TM} was connected together with the water tank. The valve (normally closed) was used to control the amount of water let through to the nozzle in the chamber. Pneumatic actuation was accomplished by open-to-air return spring, with air pressure varying of 3 to 6 bar depending on the system pressure.

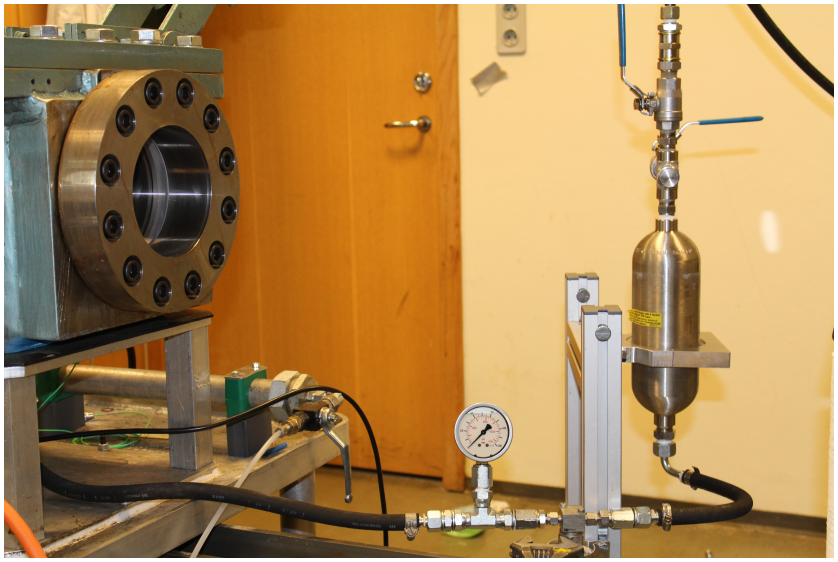

Figure 4.6: The mounted water cylinder and manometer connected to the explosion chamber.

To ensure a methodical process system, the water delivery system had to be added to the triggering system utilizing a solenoid valve and coil. The EV250B 2/2-way solenoid valve operated within 0-10 bar was paired with a 24 V coil. With the data acquisition module generating a 5 V pulse, an amplifier was required to boost the electrical charge up to 24 V. With the aid of Werner Olsen, a pulse amplifier using two transistors was constructed converting the 5 V pulse into 24 V, see Fig. 4.7. Transistors are semiconductor devices designed so that a small electric current at one end (an input voltage) produces a much bigger current (an output voltage) at the other end.

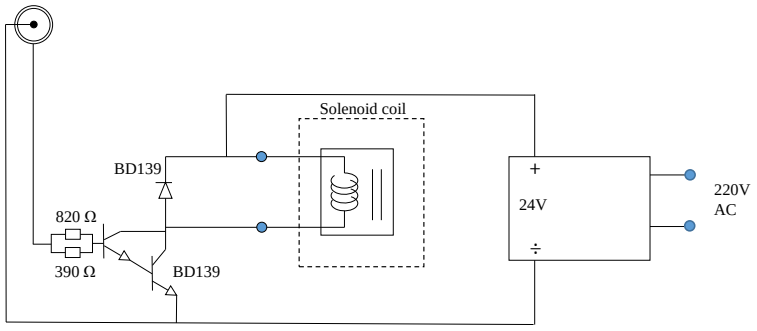

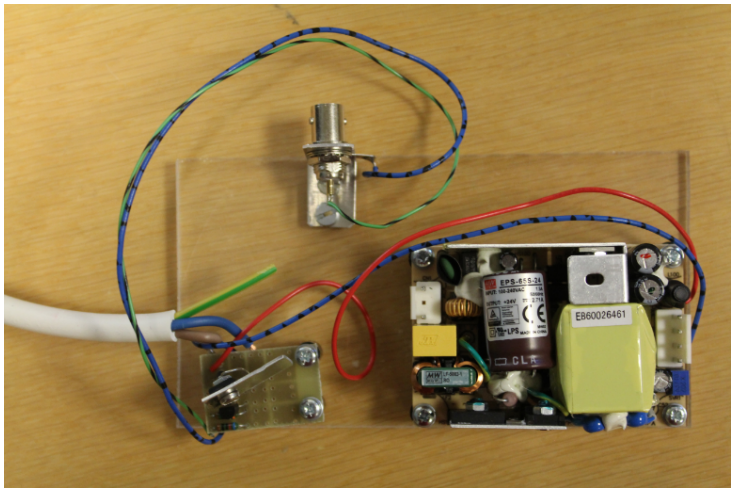

Figure 4.7: Circuit diagram and photograph of the pulse amplifier.

This amplification makes it possible to add the water delivery system to the triggering system, with negligible delay between the triggering system and the valve. Thus, as presented in the final set-up sketch in Fig. 4.8, the coil would then receive a pulse from the data acquisition module (1), converting the electrical energy into lateral motion opening the valve. Once open, pressurized air would follow through to the pneumatic actuator (2), opening the valve giving leeway for high-pressured water to pass through to the nozzle in the chamber and atomize into mist (3).

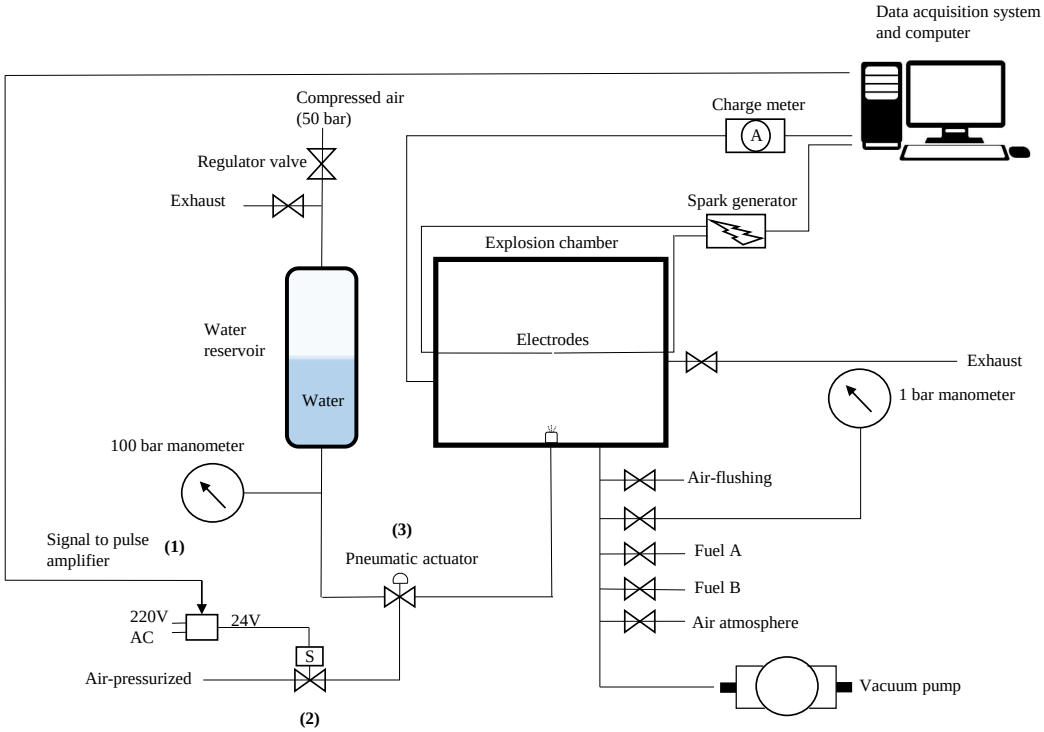

Figure 4.8: Sketch of the experimental equipment and set-up used, excluding the optical system.

4.5 Experimental procedure

4.5.1 Initial check and general practise

First of all when in the laboratory, it was important to inspect that all the equipment such as the cables, camera or the mirrors had not been tampered with. Any adjustments done on the angles of the optical system or the camera position would require re-alignment reattaining a new pixel-to-centimetre ratio as described in Sec. 5.1.1. Furthermore, once all the equipment had been turned on, it was important to test that the triggering sequence activated the camera, spark generator and pressure sensor as set up. This was to prevent a

situation whereby no spark was generated, or that the camera did not record with a flammable mixture in the chamber. Once the initial check had been completed would testing begin.

4.5.2 Procedure with hydrogen-air explosion

1. The chamber was evacuated to a desired underpressure needed for a specific equivalence ratio, and the valve closed after to let the pressure settle and be written down.
2. The needle valve leading to hydrogen was opened, and the pressure increases inside the vessel was observed until atmospheric pressure was reached. The pressure was allowed to settle, and the final resting partial pressure added was written down. This was to account for the actual mixture of hydrogen and air in the chamber.
3. All valves were checked to make sure that they were indeed closed and that the chamber was completely isolated.
4. In the PVF software, the camera setting was set to 'triggering in'. The charge meter was also activated by pressing the 'measure' button, for pressure measurement.
5. The triggering sequence was initiated after a waiting period $\approx$ 30-45 s. Once an explosion had occurred, the exhaust-valve was opened for the combustion products to exit. Soon after, the valve leading to compressed air was opened and the chamber flushed continuously for about five minutes.
6. While the chamber was being flushed, the video file with the images were saved, the pressure data was catalogued and saved, and soon a new round of test could begin.

Once done in the laboratory and leaving for the day, it was very important to make sure that all the valves controlling the fuel gas and pressurized air gas were closed. Closing all valves leading into the chamber was also essential to prevent an explosive atmosphere in the chamber, in case of a leak from the fuel gas while absent. Room temperature was usually around 294 K, and to ensure that this temperature varied as little as possible, the windows were usually opened a little during the day to compensate for temperature increase from equipment from the high-speed camera and computer. Once leaving the room for the day, all equipment was turned off and the windows were closed.

4.5.3 Procedure with hydrogen-air explosions including water mist

Adding water mist to the mixtures, some preceding preparations were required. Water from the tap ($\approx 18^\circ$ C) was filled into the water reservoir, and pressurized to desired pressure of 50 bar. Once the triggering sequence was modified to include the opening and closing of the high-pressure valve, the procedure was followed as listed in Sec. 4.5.2. After the vessel has been flushed however, the lid of the chamber was unscrewed to wipe dry the outlying remainder of water present within. Only after it was cleaned dry, and the lid screwed and tightened back into place could a new round of test begin.

Chapter 5

Post-processing

This section describes the process after the experimental procedure had been executed: from images captured and pressure values into experimental data. Both methods of finding the individual burning velocity for dry tests, by CVM and CPM, were based on the same tests. This was to eliminate any differences and uncertainties like initial pressure, temperature and air-fuel ratio. Tests done with water mist were later conducted to best match the air-fuel ratios for hydrogen-air tests.

5.1 Obtaining laminar burning velocities from the schlieren optical images

The video file recorded with the high-speed camera for each test were saved as a series of grayscale frames in .tif format. These images showed the development from pre-ignition, to the flame front propagating outwards towards the edges of the windows in the chamber.

5.1.1 Image processing

It was imperative to find an efficient way of analysing the images and finding the value for the flame radius, as each test produced an amount of 100-200 images including activity prior to and post ignition. Pugh [47], working on a similar case of spherically expanding flames, developed a code in MATLAB to computationally analyse the images, with a detailed description of the code

outlined in his work. The code with a few altercations was used for the work in this thesis and a short depiction is given below.

The software uses an algorithm to convert the grey scale intensity value of each pixel from the image into a numerical array. If the pixel intensity exceeds a specified threshold value, an edge is assigned. If an edge is detected, its pixel value was 1 and otherwise, the pixel value remains 0 effectively creating by definition a binary image, as seen in Fig. 5.1.

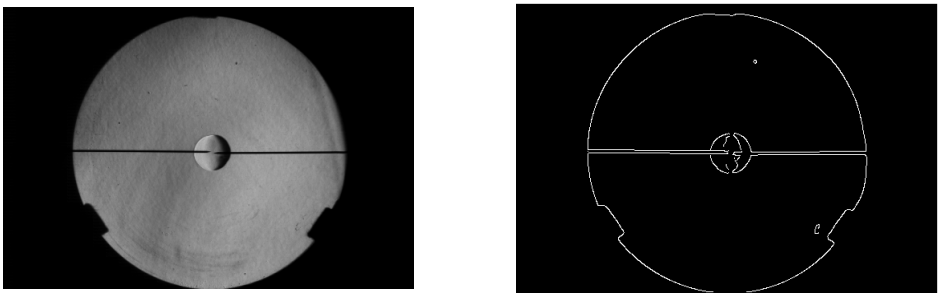

Figure 5.1: Schlieren and corresponding binary image.

Initially, a binary image showing the electrodes and other minor noise was produced and subsequently subtracted numerically from the remaining analysed images. This ensured that only the spherical outline of the flame was displayed and further analysed. The binary image of the spherical flame was then horizontally cropped to minimize the number of pixels to be analysed, as shown in Fig. 5.2. The edge pixel position of the flame was detected on both sides and saved in an Excel spreadsheet. As the images were being analysed proceeded, the edges expanded and the difference between the edges represented the diameter in pixels.

Figure 5.2: Cropped binary image just under the electrodes to extract the diameter measured in pixels.

In order to further analyse the results of each test, a pixel-to-centimetre-ratio had to be attained. This entailed capturing individual frames of known

distances using a calliper, and computationally measuring the number of pixels correspondingly giving a ratio value between pixels and centimetre. An example seen in Fig. 5.3, gave a ratio of 0.0402 pixel/cm, using a calliper with a width of 1.150 cm. This procedure was done three times to ensure a legitimate ratio, and eliminate any uncertainty.

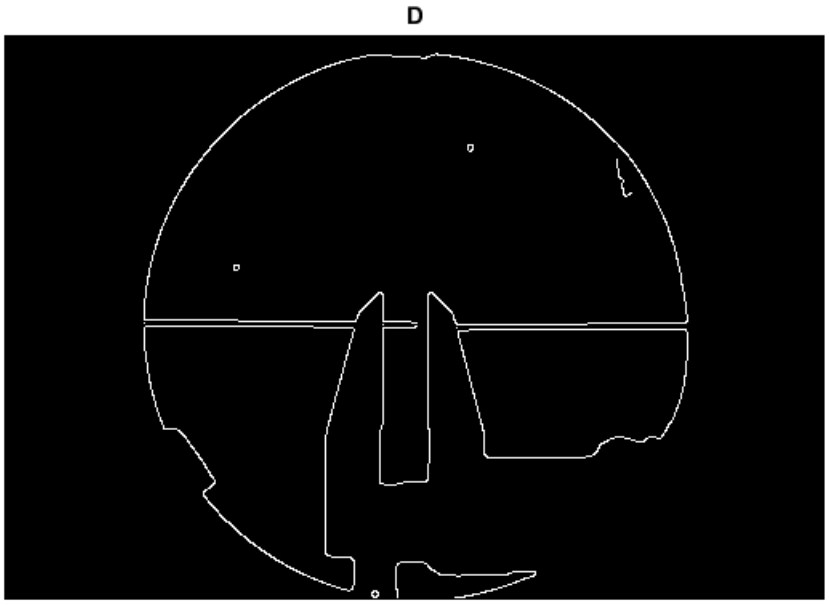

Figure 5.3: Calculating the pixel-to-centimetre ratio, using a binary image of a calliper with a known distance between the pivoted legs of 1.150 cm.

5.1.2 Determining valid range of extrapolation

To illustrate the numerical processing methodology, a single hydrogen-air test will be used as an example hereafter. A test carried out at the equivalence ratio of 1.50, ambient temperature of 294 K and atmospheric pressure (1 bar) produced data for the radius plotted against the time data for the images.

Prior to plotting the expanding radius using CPM, a valid range of extrapolation had to be decided upon. A radius too small would be influenced by the ignition energy, when substantially above the minimum ignition energy. The spark plasma induced expansion and conductive energy transfer from it may lead to an exaggerated flame propagation. Subsequently, a radius too

big would be influenced by the chamber confinement due to the restriction of the flow of the unreacted gas and would also be regarded inaccurate. A pressure increase more than 1% of the initial pressure was to be withheld, with the constant pressure assumption being justified. Ideally to determine the ignition and unsteady effect, experiments on the hydrogen-air mixture at fixed equivalence ratio but different ignition energies would be conducted. But the impracticality of modifying the spark generator each time would make the effort too time consuming, considering the time frame involved in this thesis. Therefore, other determination methods had to be invoked. However, there is not a systematic study to determine the proper low bound radius uninfluenced by the ignition energy, and most researchers base the choice on intuition without any appropriate justification, observed by Chen et al [48]. In the work of this thesis, comparing choices made in different literature, and considering an ignition energy of 3.27 mJ and $R_v = 8\ cm$ in this work, a lower bond radius up to 11 mm was neglected to mitigate the ignition-affected, early stage flame propagation for all hydrogen-air mixtures.

Burk et al. [49] suggested that the effect of confinement could be neglected for flame radius less than 30% of the wall radius, while still achieving acceptable accuracy. Therefore, with a radius of the chamber being 169 mm, a maximum radius of 40 mm constituting 26% of the volume radius was used to minimize the influence of confined reactant pressure rise. A propagating schlieren flame radius is plotted against time in Fig. 5.4. This range constitutes ≈ 30 data points, the least number of points necessary to converge a representative third order polynomial equation.

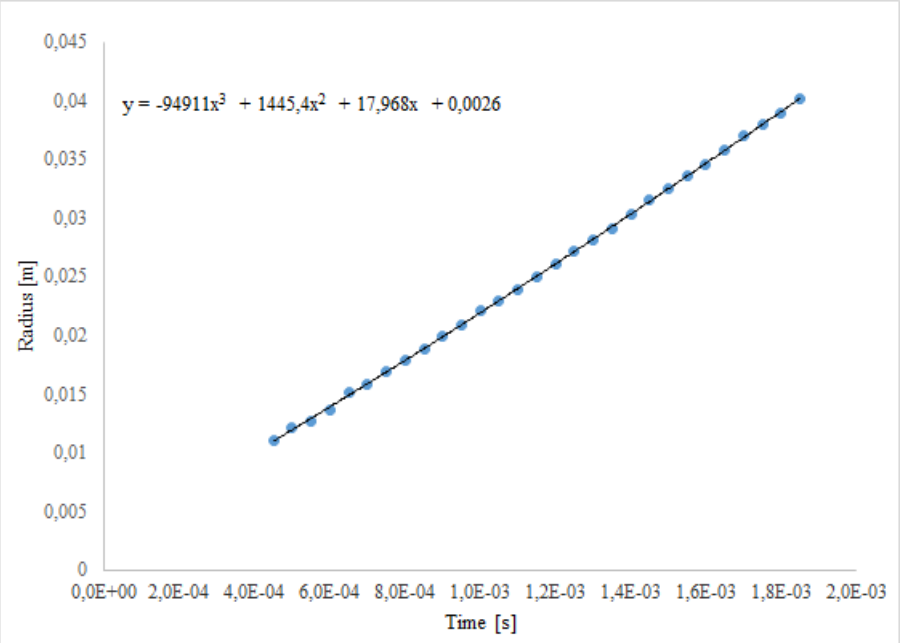

Figure 5.4: Flame radius with time after ignition within the valid range of extrapolation, showing a third-order polynomial equation.

5.1.3 Linear extrapolation methodology

Presented in Eq. (2.15), this technique uses the relationship between the stretch rate and the flame speed. Simple to employ by regressing a linear fit to the plotted data, the required coefficients such as the unstretched flame speed and the Markstein length were obtained. The third order polynomial regression retrieved from the $r_f - t$ relationship presented in Fig. 5.4 was further utilised in finding the corresponding flame speed. By differentiating the polynomial and applying Eq. (2.10) and Eq. (2.14), a representative flame speed uninfluenced by stretch was read by the coefficients. Fig. 5.5 shows the S_f and α plotted against each other with a linear relationship superimposed, and extrapolated to the condition of zero stretch. The Markstein length, L is the slope of the line, -0.0014 m, and the unstretched flame speed, S_{f_u}, where the trendline intersect with the vertical axis: 23.416 m/s.

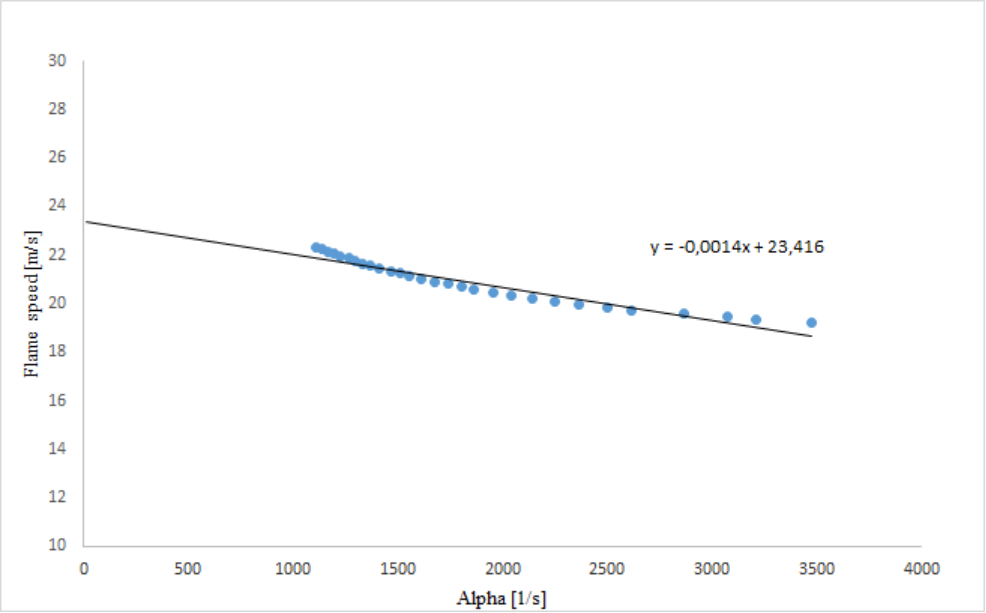

Figure 5.5: Propagating flame velocities plotted over the stretch rate curve and a fitted linear extrapolation.

5.1.4 Non-linear extrapolation methodology

A least square non-linear regression was used after rearranging Eq. (2.16) to

$$\left(\frac{S_{f_s}}{S_{f_u}}\right)^2 ln\left(\frac{S_{f_s}}{S_{f_u}}\right)^2 + 2\frac{L\cdot\alpha}{S_{f_u}} = 0, \tag{5.1}$$

in order to determine the two constants of the fitting, namely S_{f_u} and L. The initial input values for the aforementioned constants were the values found in Sec. 5.1.3. The best-fit curve minimizes the sum of squared residuals and discontinues when the least squared error is as small as possible. An analysis was done by Coronel et al. [50] looking into the sensitivity of the non-linear least square fit to the initial guess. They suggested not only having one guess per parameter, but rather up until 10 initial guesses to minimize the error. In this thesis, an effort was made to make up until five initial guesses close the S_{f_u} value found with the linear extrapolation, until the final value was within 5% of the previous value. The result of a non-linear extrapolation is shown in Fig. 5.6. This association yielded the unstretched flame speed to 23.1 m/s with the corresponding Markstein length being -0.0010 m.

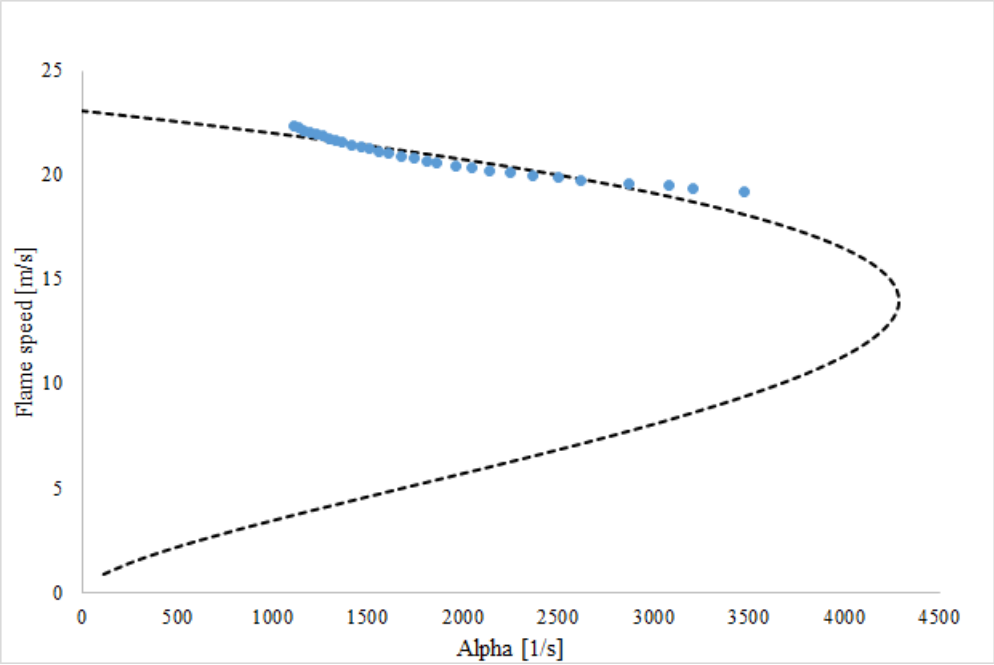

Figure 5.6: Propagating flame velocities plotted over the stretch rate curve and a fitted non-linear extrapolation.

5.1.5 Calculating the expansion ratio

In order to transform the unstretched flame speed to burning velocity using Eq. (2.11), the expansion ratio describing the adiabatic density was required. These were acquired by using an online Chemical Equilibrium Calculator (CEC) developed at Colorado State University [51]. The method implements the STANJAN algorithm developed by Bill Reynolds, using data from the Chemkin thermodynamic database. Assuming a mixture of ideal gasses and condensed phases are ideal solutions, it provides a superior means for solving chemical equilibrium state property solutions such as pressure, temperature and enthalpy. The user selects the species to be included in each phase of the system, sets the atomic populations and state parameters, and CEC solves the equilibrium state.

In this case, constant pressure and enthalpy was chosen, and 1 bar and 294 K for pressure and temperature respectively. A list of elements present in the reaction, H, O and N was required together with the mole fraction of each reactant used, $H_2 = 1$, $N_2 = 1.252$ and $O_2 = 0.333$. A list of species present at equilibrium was specified as H_2O, H, NO_2, OH, H_2 and NO. Using the

CEC to calculate the initial and equilibrium state for a specific hydrogen-air mixture, the following relation was used:

$$E = \frac{\rho_u}{\rho_b} = \frac{\frac{1}{V_u}}{\frac{1}{V_b}} = \frac{V_b}{V_u}. \tag{5.2}$$

An example using the CEC is shown in for $\phi = 1.50$ is shown in Fig. 5.7. V_u being 1323.5 cm^3/g and V_b being 8814.6 cm^3/g, the calculated expansion ratio (E) was 6.66. This could be further used to calculate the burning velocity from the linear flame speed of 23.416 m/s found in Sec. 5.1.3. The laminar burning velocity was 3.52 m/s. Using the non-linear flame speed found in Sec. 5.1.4, the laminar burning velocity was found to be 3.50 m/s.

	Initial State	Equilibrium State
Pressure (atm)	9.8692E-01	9.8692E-01
Temperature (K)	2.9400E+02	2.2436E+03
Volume (cm^3/g)	1.3235E+03	8.8146E+03
Enthalpy (erg/g)	-6.4373E+07	-6.4373E+07
Internal Energy (erg/g)	-1.3879E+09	-8.8789E+09
Entropy (erg/g K)	9.6137E+07	1.2244E+08

Figure 5.7: Various initial and equilibrium state calculated results by CEC.

5.2 Obtaining values from the pressure measurements

Typically high-frequency noise occurs in electronic recording devices formed by random disturbances in the electrons designated pathway. These strays influence the voltage of the output signal and thus create detectable noise. To prevent the noise in the raw pressure data from being amplified during further calculation, the raw data was passed through a filter. A Savitzky-Golay smoothing filter is used to "smooth out" the raw pressure data. The filter is optimal in the sense that it minimizes the least-squares error in fitting a polynomial to frames of noisy data. A third-degree polynomial and a data window involved 31 points to unsure suitable smoothing, namely 15 on the

left and 15 on the right of the point of where the mean value and its first derivative was to be evaluated. Pressure data obtained from the specified mixture ($\phi = 1.50$) showing the pressure increase as a function of time is plotted in Fig. 5.8. It shows the raw pressure data, and its filtered values. A magnified portion of the data is shown to illustrate the oscillating nature of the raw pressure data.

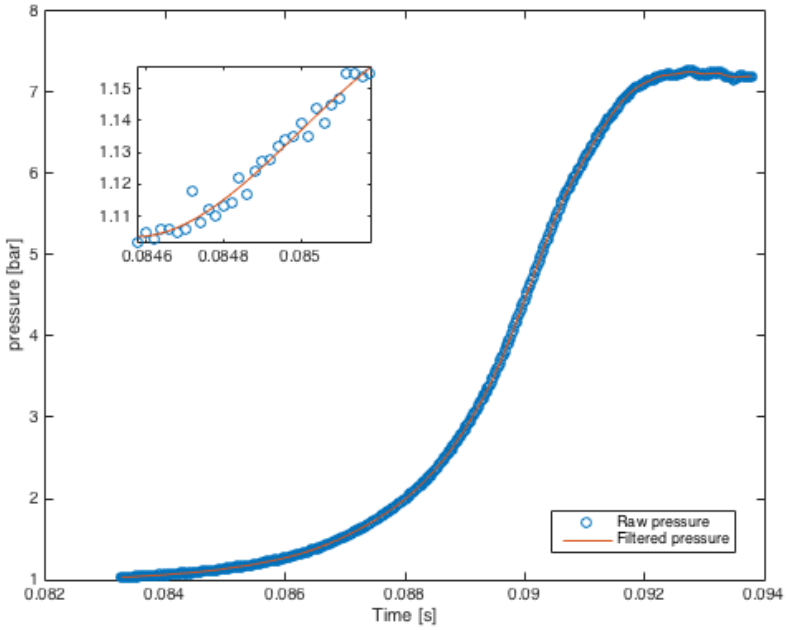

Figure 5.8: Internal chamber pressure-time history data for a hydrogen-air mixture, showing both raw and filtered pressure data.

Initially, Eq. (2.17) was to be used to find the S_u, as a function of both pressure and flame radius. But two drawbacks made it practically unusable. The first drawback was that it required simultaneous and synchronized flame front filming and pressure monitoring. In this case, with the pressure being monitored with a frequency of 50 000 Hz and the images taken at 20 000 fps, synchronizing these two magnitudes would be impossible without compromise in data. The second drawback related to the inaccuracy-amplification, due to the similar dimensions of the two terms in Eq. (2.17). The evolution of flame is obtained when the pressure is negligibly low, and the evolution of chamber pressure is evident when the flame radius is large enough. Consequently, the flame radius would therefore have to be significantly large, and pressure rise significantly low for the determination of (dr_f/dt) and (dp/dt) to be aligned.

With raw data noise and range constraints to consider, a larger combustion vessel would have to be employed as done by Fiock and Marvin [24] ($R_v = 16\ cm$) to hinder inaccurate values affecting the resulting S_u values found.

The filtered data was therefore applied only Eq. (2.19) to find S_u values as a function of the pressure. The required thermodynamic properties γ_u and γ_b however, was first to be determined. Eq (2.9) rearranged using Eq. (2.7) became:

$$\gamma = \frac{C_{p_i}}{C_{v_i}} = \frac{C_{p_i}}{C_{p_i} - R_s}. \tag{5.3}$$

Properties γ_u and γ_b could then be calculated at initial and equilibrium temperature, with the latter being found using CEC with the same procedure described in Sec. 5.1.5. The results used along with Eq. (2.25) was used to find the laminar velocity at initial conditions. This is done practically by fitting the S_u values by a non-linear least-square solver to a rearranged Eq. (2.25),

$$\frac{S_u}{S_{u_0}} - \left(\frac{p}{p_i}\right)^{\alpha} = 0. \tag{5.4}$$

Fitting the values from S_u required a pressure range first and foremost to prevent effects of chamber confinements in addition to the influence from ignition energy. Simultaneously, other considerations must be set. To start with, Eq. (2.19) was highly sensitive to low-pressure data due to the differential term (dp/dt). Any noise causing an unsteady rate of pressure rise caused S_u to produce magnified nonsensical values. Therefore the lower limit of pressure measurements was set to 2 bar, 30% of the total pressure measured. The upper limit was set up to 4 bar, 64% of the total pressure measured, corresponding to the inflection point where the pressure derivative maximizes and the heat loss was not to be neglected any more. The Savitzky-Golay smoothing filter would accordingly be applied within the valid range of pressure, with the initial and final 15 points not accommodated, due to missing number of neighbour data points on each respective sides. This premise leads to a more narrowed pressure range extrapolated, but is kept consistent through all the calculations and is therefore not further corrected.

Fig. 5.9 shows the S_u data fitted to Eq. (2.25) within the pressure range established, extrapolated back to the initial pressure defining S_{u_0} as the planar

laminar burning velocity at initial pressure[1]. Once extrapolated, S_{u_0} could be obtained, or here also read straight from Fig. 5.9 as 3.48 m/s.

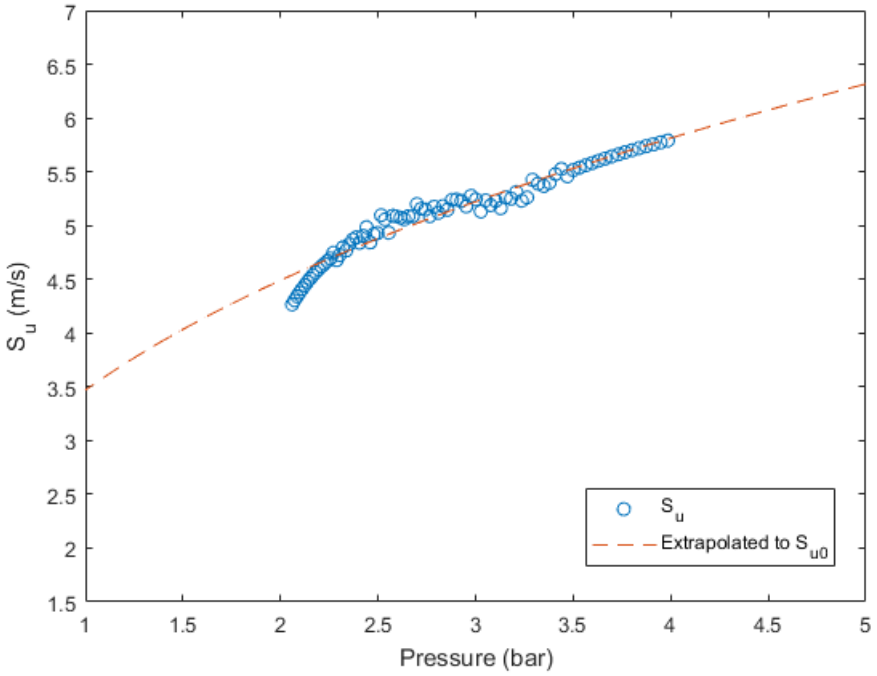

Figure 5.9: The laminar burning velocity obtained as a function of pressure, and the extrapolation back to initial pressure, S_{u_0}.

[1]Used in Eq. (2.20) and (2.22) instead of the experimental measured p_{max}, the calculated adiabatic isohoric equilibrium combustion pressure ($p_{max,ad}$) was used in calculating S_u.

Chapter 6

Results and discussion

In this chapter the experimental results are presented. Prior to this, some of the measures taken to install and perfect the experimental set-up are presented. When reviewing the laminar burning velocities, all the data for each test presented onwards (55 in total) are bestowed in full detail in Appendix A, including the values found using CEC.

6.1 Preliminary test and optimization

6.1.1 Restoring the chamber

A suspicion concerning leakage in the chamber was first attended to, as it would lead to inaccuracy in the gas-mixing system, which had to be sealed. In addition, a leakage from the explosion chamber over time could in a worst case scenario lead to a flammable atmosphere in the laboratory. Filling the chamber up to a significant amount of overpressure, a gas leak detector in form of soap mixture was used to wet down suspected parts and with the formation of bubbles, leakages were found and sealed. A leakage rate of 0.0005 bar/min was found, acceptable for use in the work in this thesis, as mixture and ignition would fall within the time frame of 1-2 min.

New electrodes were installed, eliminating any conductor disturbances in the current distribution. The electrodes replaced were of same dimensions in size and spark-gap, to accommodate the combination of needed spark energy, and thin electrodes to avoid exceeded influence on the onset flame propagation. In the preliminary stage of testing, the windows broke as result of being

mounted in too tight, and new windows had to be bought for replacement. New windows also meant removing any irregularities and scratches on the previous glasses installed.

6.1.2 Assembly and alignment of the schlieren optical system

The assembly and positioning procedure for a z-type schlieren system is discussed earlier in Sec. 2.5.2. Due to the nature of the schlieren optical method, any misalignment, optical imperfection or incorrect apparatus adjustment impacts the quality of the captured images. Attaining a good schlieren image requires therefore effort and diligence to set the system up carefully at the outset.

The first alignment issue regarding the height of the horizontal plane was already rigged, with mounting benches supporting the chamber, mirrors, and the light source system. The mirrors, held by two metal sticks, were made including marked lines for measurement of height, therefore making it easy to match both mirrors, not only to the same height, but also to the height of the circular chamber windows. After that, the rest of the equipment such as the light source system, knife-edge and the high-speed camera could be adjusted accordingly to the same height.

Instead of a traditional single knife-edge, a double knife-edge system or a glass sheet with an opaque white-dot can be located at the focal point of the second mirror. This ensures a sharper and brighter contrast compared to the image produced using a single knife-edge [23]. This was not possible to implement in this case, due to astigmatism. Astigmatism is described in detail by Settles [27], but in short terms it causes the light to non-coincide in a common focal point. This is due to the off axis rotation of the two mirrors, creating two focal points instead of one, which is common in z-type set-ups. This effect can be reduced but not entirely negated by using small offset angles between the light source, mirrors and camera, and arranging a long length (twice the mirror focal length) between mirrors.

Carrying this out, the offset angles were reduced as much as possible, though due to space restrictions in the laboratory the length between mirrors could not be extended. A study done by Prescott [52] suggested using a plano-cylindrical lens between the light source and the first mirror to summon a common focal point. He was then able to use either a vertical or horizontal knife-edge at the same position along the optical axis, as the light beam at the

focal point was reconciled. An attempt using a plano-cylindrical lens did not yield positive results. The astigmatism did subside a little as the focal point became more rounded signalizing less split between focal points. However, the images of the expanding flame became unclear and the MATLAB-code was unable to detect the flame edge and successfully extract the propagating flame velocity due to the obscure flame-edge, see Fig. 6.1. As a result, it was only possible to use only a vertical knife-edge in the position corresponding to a stigmatic image.

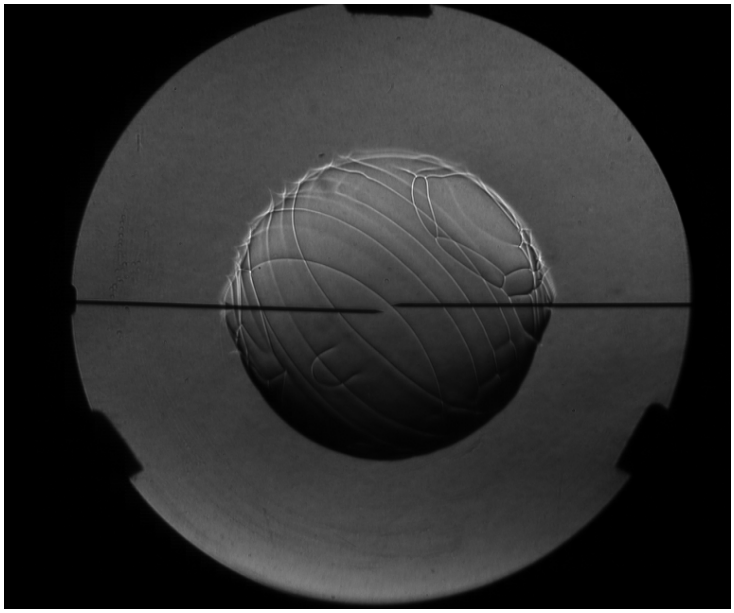

Figure 6.1: An expanding flame image taken, using a plano-cylindrical lens between the light source and the first mirror to reduce astigmatism. A fuzzy flame edge is exposed.

6.1.3 Validating the pressure transducer

Every pressure transducer produced has its unique calibration depending on its range of pressure. Regarding the pressure transducer used in this work, it was last calibrated in 2009 within a range of 0-25 bar.

An informal quality control of the pressure transducer was conducted to determine its accuracy using a secondary pressure source. This was done at GexCon, using an air reservoir fitted with a VDO OTA Manometer (0-10 bar). The pressure transducer was mounted to the reservoir, but separated by a manual valve. The test consisted of filling the reservoir to a given pressure

using compressed-air, and opening the ball valve allowing the known pressure to also be measured by the pressure transducer. The pressure input was measured visually and accordingly, the results attained were modest and served only as an indicator of the transducers accuracy. Presented in Tab. 6.1, all four test gave good agreement with a maximum discrepancy of maximum 0.7%.

Table 6.1: A quality control of the pressure transducer using a manometer as a secondary pressure source.

Test	Pressure gauge (bar)	Transducer (bar)	Difference (%)
1	3.94	3.94	0.0
2	4.90	4.92	0.4
3	5.95	5.99	0.7
4	6.93	6.92	0.1

6.2 Estimation of laminar burning velocities

6.2.1 Results from CPM

The results of the expanding spherical flame experiments are presented in this section. Seven equivalence ratio in the range between $\phi = 0.7$ - 1.9 (22.7% - 44.4% hydrogen in air by volume), avoiding near-flammability-limit mixtures, were tested for hydrogen-air combustion, under initial ambient conditions of 294 K and atmospheric pressure(1 bar).

To illustrate the test being analysed, a sequence of frames of an expanding spherical flame are shown in Fig. 6.2, for the least, middle and largest equivalence ratio giving a holistic impression. A clear flame front illustrated with a clear background, displaying a clear distinction between flame and background is apparent, being a prerequisite for the MATLAB-code to be used. At the outset, the images obtained at equal time steps show varying spherical flame development, slowest for the lean mixture illustrated by the relative smallest flame diameter especially after 3 ms. Both rich mixtures show faster flame propagation, $\phi = 1.3$ being the fastest.

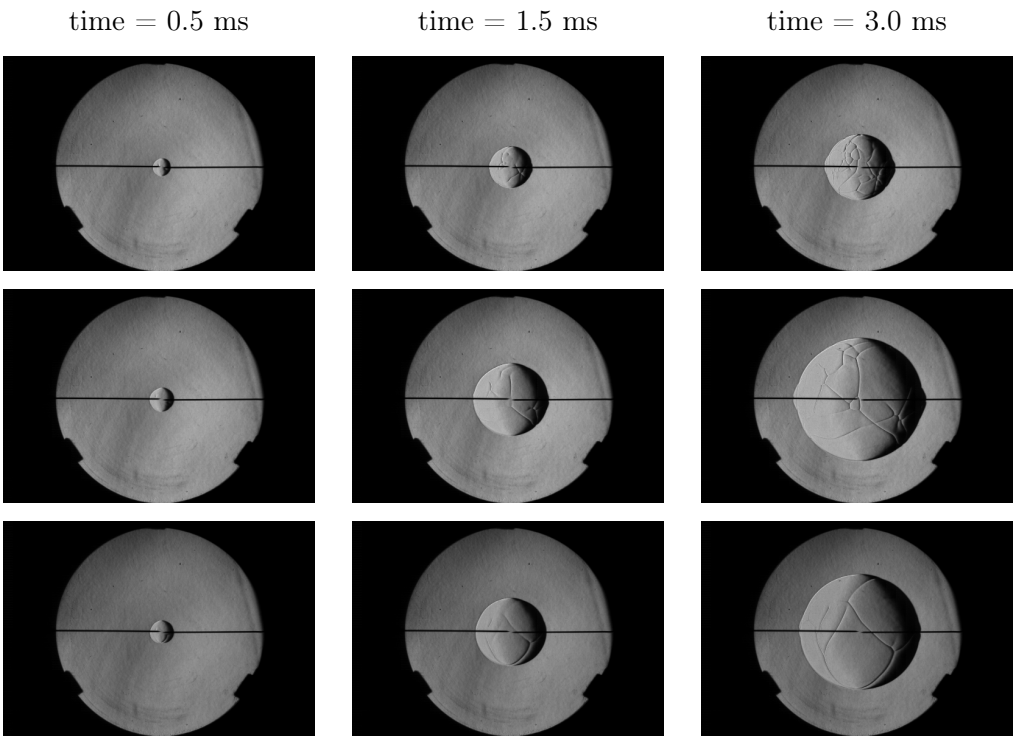

Figure 6.2: Captured sequence of schlieren images showing expanding flame propagation for equivalence ratios $\phi = 0.7$, 1.3, 1.9 from the first row downwards respectively.

Inspecting the images further, two things become apparent. First, diffusion between the air and fuel is sufficient. Flame propagation is seen spherically and symmetrically in all directions for the three mixtures, in all three time steps. For hydrogen, being both with high reactivity and diffusivity, poor mixing would result in buoyancy effects driving the flame propagation upwards, and which is absent in this case to show that sufficient mixing is attained. Secondly however, there are signs of wrinkling in all cases. This could be due to hydrodynamic or thermodynamic instabilities i.e. movement in the gas phase due to non-quiescent conditions when ignited, causing an increase in the flame propagation velocity as a consequence. An investigation of instabilities of hydrogen-air outwardly propagating spherical laminar premixed flames was done by Bao et al. [53]. According to this study, hydrodynamic instabilities were always present and decreased as the concentration of hydrogen increased. The source of instabilities was due to irregular distortions of the flame surface, and occurred when the flame radius was large enough and the diffusion stability not able to offset its effect.

Fig. 6.3 shows a comparison of the difference in radial propagation rates for the seven tested and evaluated equivalence ratios. It demonstrates clearly the flame development for different equivalence ratio mixtures, with a linear correlation between flame radius and time for subsequent mixtures. $\phi = 0.7$ and $\phi = 1.3$ are found to have the slowest and fastest rate of flame propagation respectively. According to Huang et al. [54], the gradient of the $r_r - t$-curve reflects the stretching effectiveness of flame. For an unstable flame, the gradient will decrease with ongoing flame expansion. Thus, we can conclude that in this case with the absence of any decline, that the flame expansion for the mixtures presented are relatively stable, despite of the omnipresent hydrodynamic instabilities.

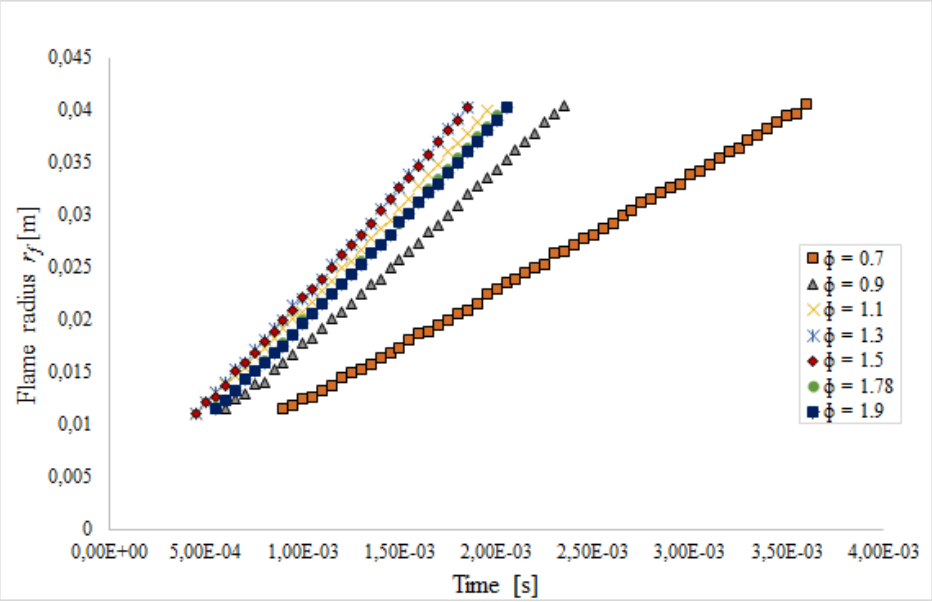

Figure 6.3: Extracted flame front radius from schlieren optical images.

Fig. 6.4 and 6.5 show the measured stretched flame speed as a function of stretch rate, with extrapolated linear and non-linear unstretched flame speed respectively. The quality of the fitting, acceptably implemented, is present for all mixtures with a decreasing flame speed found as expected when the stretch rate increases. Mostly non-linear trends in the the relationship between the stretch and flame speed are exhibited.

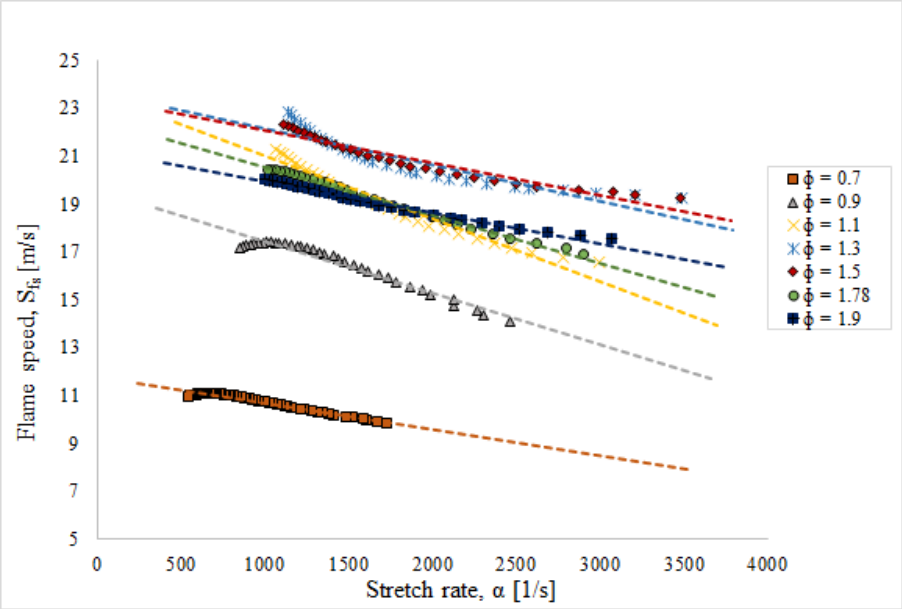

Figure 6.4: Calculated stretch rates as a function of flame speed, with linear extrapolation for extracting the unstretched flame speed and Markstein number.

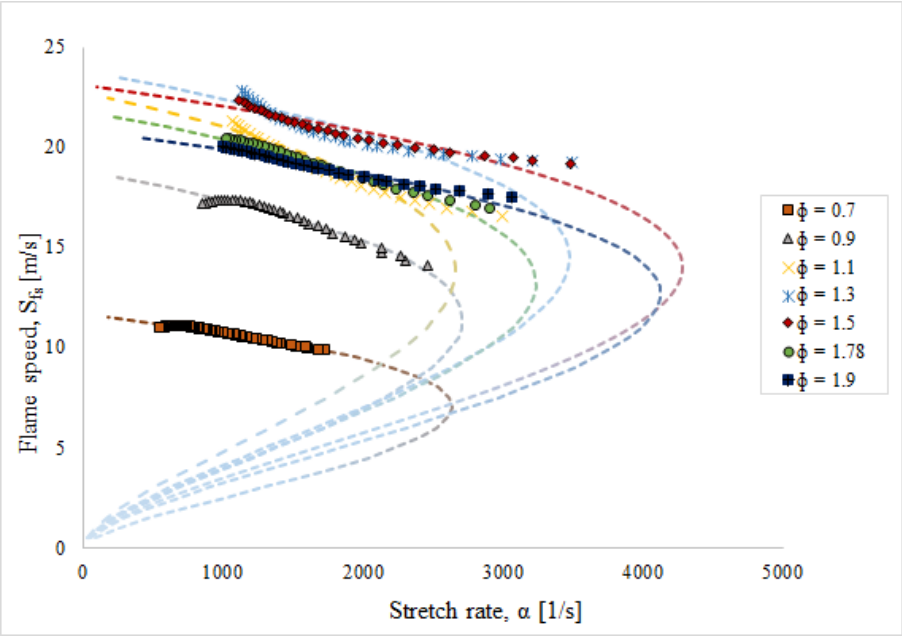

Figure 6.5: Non-linear extrapolation for extracting the unstretched flame speed and Markstein number. Extrapolation is shown as the dashed line.

Expansion ratios for all the mixtures tested were found, which is a criteria to calculating the laminar burning velocities. The methodology was used as described in Sec. 5.1.5, and all the expansion ratios for each equivalence ratios are shown in Fig. 6.6. These values represent an ideal expansion ratio, when equilibrium is attained after a prolonged amount of time. In reality, an ideal combustion may not be the case and might differ from the values obtained. Nevertheless, these values were utilized in lack of a better relation for the non-ideal expansion ratio found during the duration of this work.

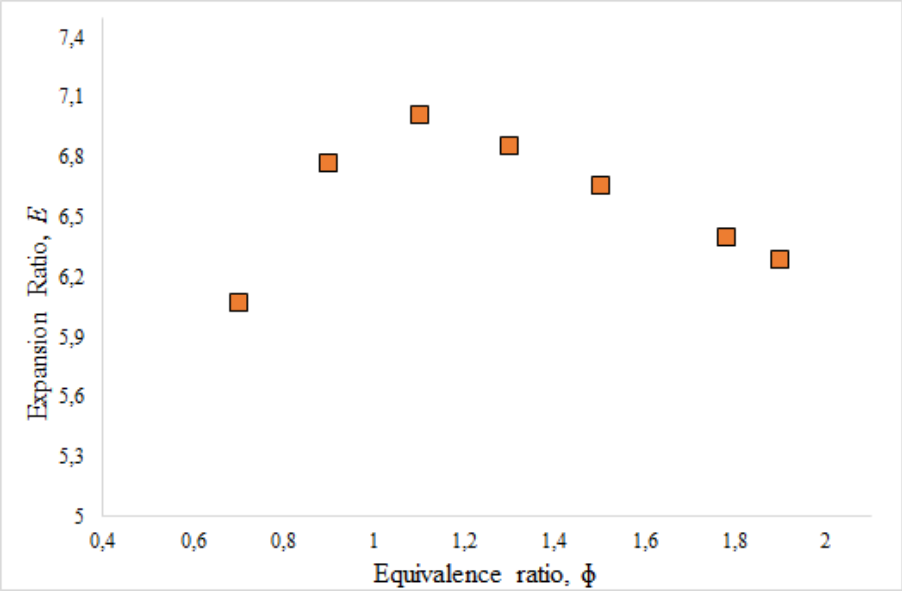

Figure 6.6: Expansion ratio for various hydrogen-air mixtures obtained using CEC.

Finally, the laminar burning velocities calculated using both the linear and non-linear method are shown in Fig. 6.7. The two extrapolation methods show little discrepancies between each other in the different mixtures, with the linear stretch relation being consistently slightly overestimated, agreeing with the previous work of linear versus non-linear comparisons [22]. The conventional linear-stretch effect assumption used to obtain the laminar burning velocity remain valid compared to the non-linear approach with hydrogen-air mixtures.

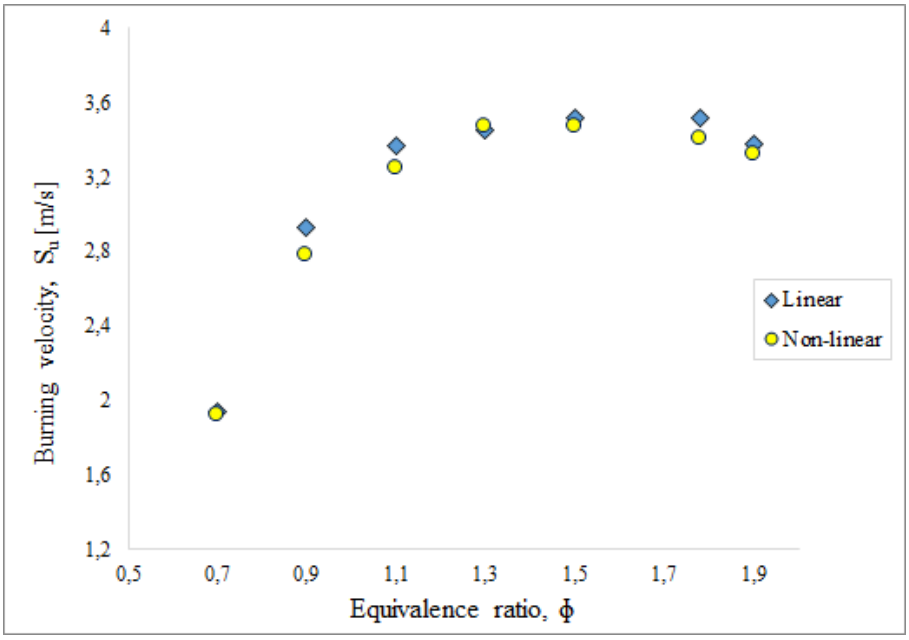

Figure 6.7: Laminar burning velocities for hydrogen-air mixtures, measured at initial temperatures of 294 K and atmospheric pressure.

6.2.2 Results from CVM

Fig. 6.8 shows the experimental pressure-time history for the seven mixtures analysed adopting the constant-volume method. A typical S-shape form can be observed for each curve, characterising the pressure period before and after reaching the inflection point. The maximum overpressure was measured at ϕ = 1.1 at approximately 8 bar.

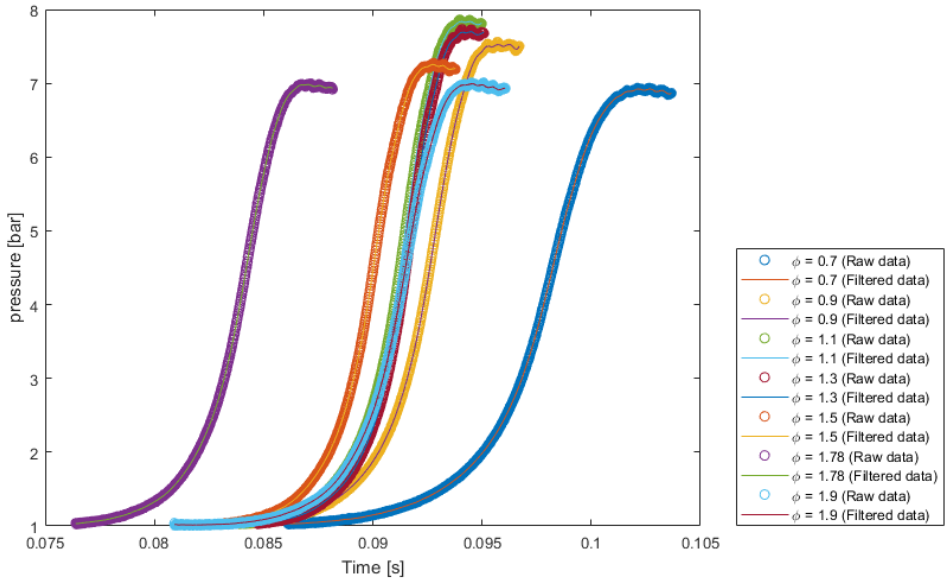

Figure 6.8: Pressure-time history for all seven hydrogen-air mixtures during the CVM combustion event, showing the raw and corresponding filtered data.

However, the maximum pressures are susceptible to lower ranges depending on the confinement. The larger the surface to volume ratio is, the lager the heat losses in the final stage of the explosion. A study done by Cashdollar et al. [55] verified this concept by tests done in a 120 litre vessel. Presented in Fig. 6.9, the maximum explosion pressure in the larger volume reaches values in the magnitude as those calculated by CEC at adiabatic equilibrium, with both peaking at the highest value of 8.3 bar for $\phi = 1.1$. Compared to the experimental values obtained from the 20 litre experiments, differences in the p_{max} values increase with the equivalence ratio of the mixture, starting from 0.3 to 0.7 bar at the richest mixture.

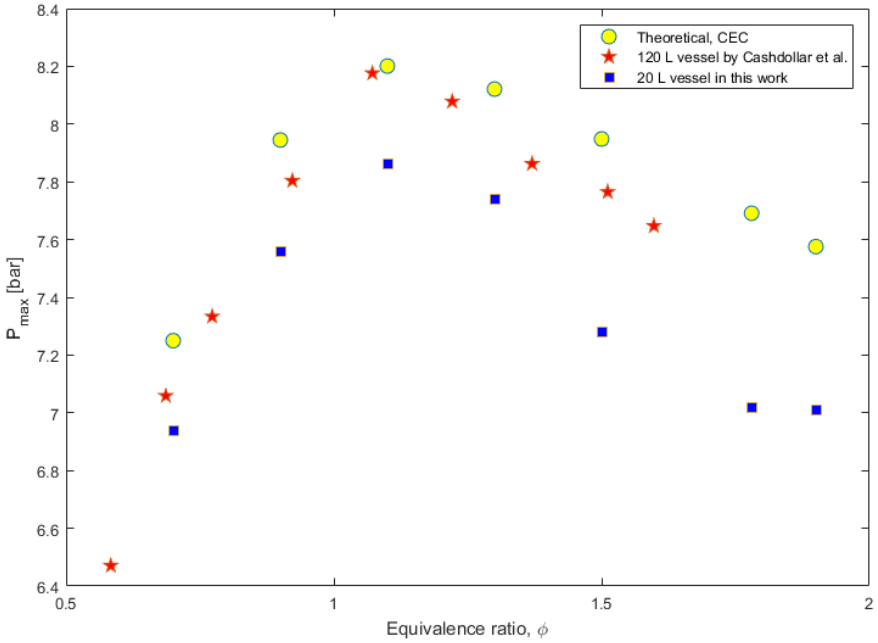

Figure 6.9: Measured maximum explosion pressure for a hydrogen-air mixture using a 20 and 120 litre vessel, used in the work in this thesis and in the work of Cashdollar et at. [55] respectively, compared to the calculated equilibrium pressure.

Using a lower maximum pressure than the ideal value, increases the calculated laminar burning velocity as it insinuates a faster achieved maximum pressure. It is therefore determined, rather than to designate the measured maximum pressure (p_{max}) as erroneous throughout the tests, to replace the value with the calculated adiabatic isochoric equilibrium explosion pressure for constant volume and internal energy calculated using CEC, now denoted as $p_{max,ad}$. Thus Eq. (2.19) is fitted using the theoretical value for maximum pressure that would be reached assuming complete combustion with no heat losses in a vessel with a constant volume. This is also to account for the ideal expansion values used in CPM obtained laminar burning velocities.

Presenting the flame radius as a function of time is shown in Fig. 6.10, using Eq. (2.18). A linear correlation between the flame radius and time is found for the different mixtures, similar to the trend found with CPM in Fig. 6.3. The calculated and corresponding extrapolated laminar burning velocities, S_{u_0}, are shown in Fig. 6.11.

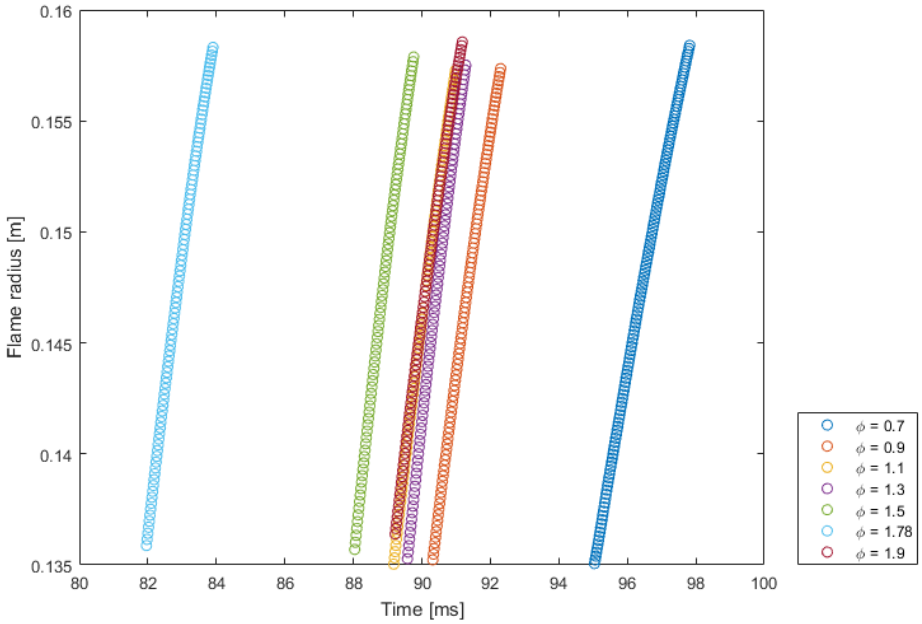

Figure 6.10: Calculated flame radius rate as a function of time, obtained from the pressure-time history.

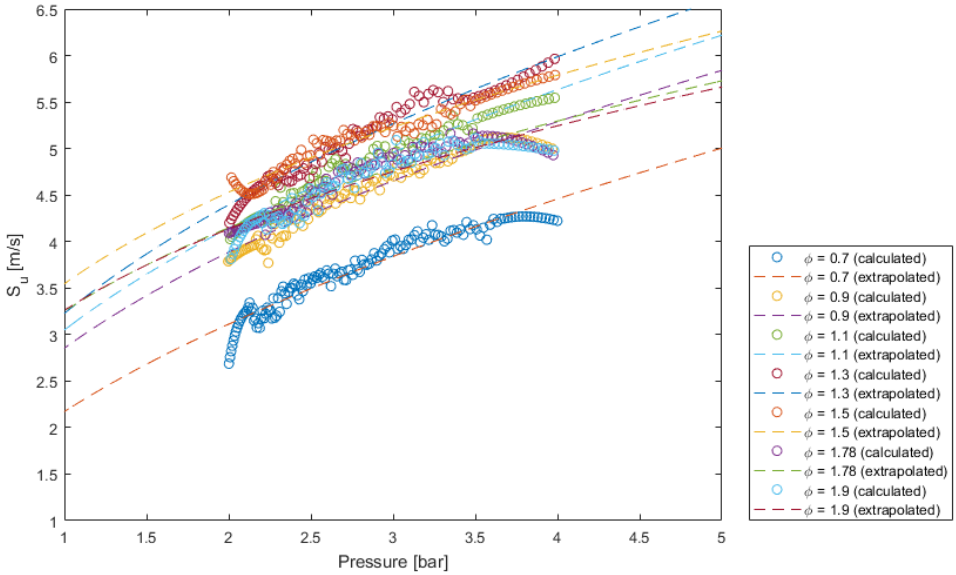

Figure 6.11: Calculated and extrapolated laminar burning velocities as a function of the dynamic pressure inside the vessel for various mixtures.

Finally, the burning velocities for the various mixtures obtained by CVM, see Fig. 6.12, compared to the velocities obtained by CPM. Both trends are in agreement, with the CVM values initially overestimating the laminar burning velocity, to later underestimating the laminar burning velocity as the equivalence ratio increases with a maximum deviation of 10 % at the richest mixture. Interestingly, for the mixture at $\phi = 1.5$, all three methods are in good agreement at peak burning velocity significantly above the stoichiometric value.

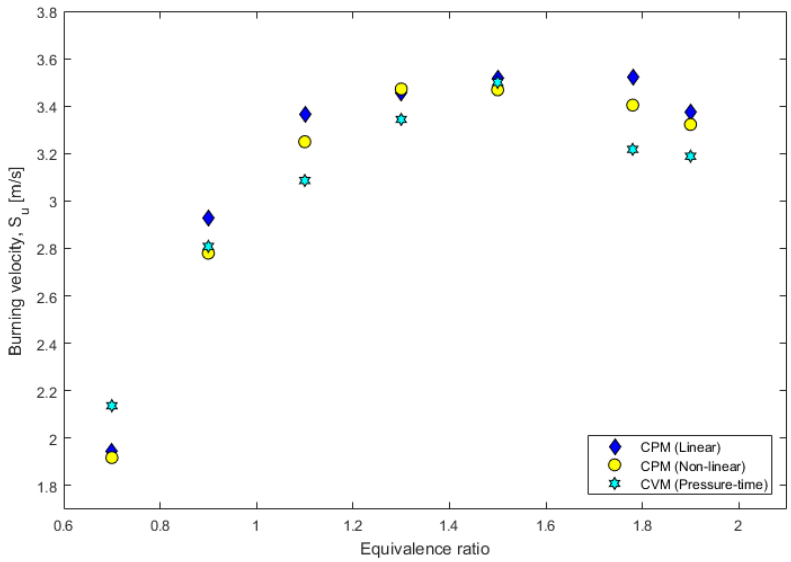

Figure 6.12: Laminar burning velocity for hydrogen-air mixtures measured at initial temperature (294 K) and atmospheric pressure (1 bar) for each of the methodologies applied.

6.2.3 Comparison with other literature data

Selected published data available are used in direct comparison with values obtained in the work of this thesis in Fig. 6.13, all illustrating different procedures used to acquire the laminar burning velocity. The measurements of Wu and Law [56], Koroll et al. [57] and Liu et al. [58] lead to as high values as those obtained in this work, although consideration of the effect of the stretch rate over the laminar burning velocity are not applied in their work. For instance in the work of Liu et al. [58], they used a small 3 mm diameter nozzle, resulting in overestimated laminar burning velocity values.

The smaller the nozzle diameter, the higher the velocities measured [34]. When the experimental determination takes into account the stretch effect, it shows lower laminar burning velocity values, displayed by Taylor [32] and Lamoureux et al. [59]. This behaviour is more evident in the fuel-rich conditions, where the uncorrected values can be up to twice the values of the stretch corrected values. Interestingly, Dahoe [14] obtained laminar burning velocities using the CVM method in proximity of the conservative values whereby stretch had been accounted for. Therefore, for the values obtained in this work, the development of wrinkles as observed in Fig. 6.2 could be the source of the higher laminar burning velocities, influencing both the constant-pressure and volume methods of obtaining the laminar burning velocities.

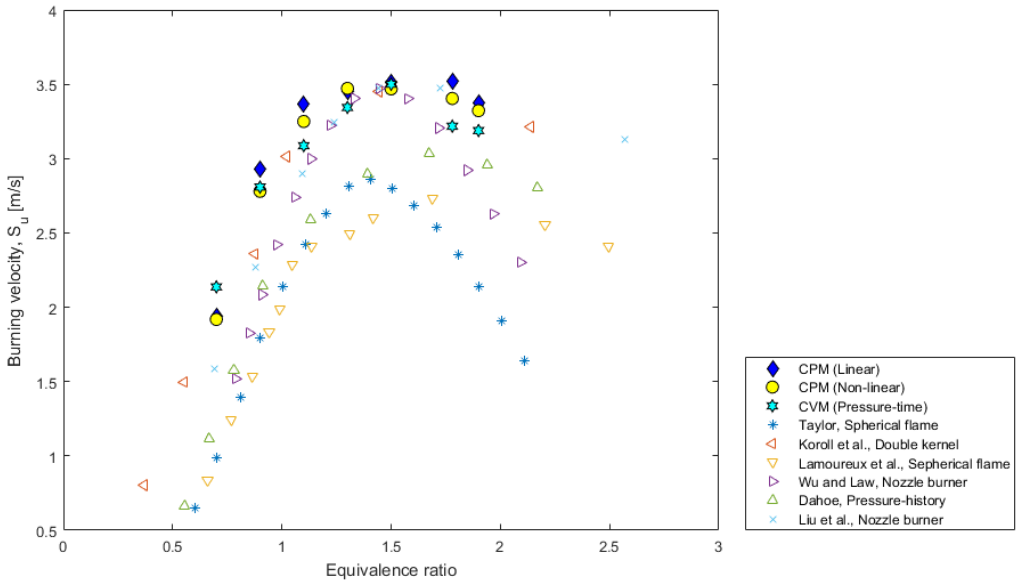

Figure 6.13: Comparison of laminar burning velocities measured in this work, and by other authors using various techniques in hydrogen-air mixtures at atmospheric pressure and room temperature.

6.3 Estimation of burning velocity with hydrogen-air mixtures exposed to water mist

Similar to the hydrogen-air mixtures described in Sec. 6.2, seven equivalence ratios in the range between ϕ = 0.7-1.9 were tested under initial ambient con-

ditions of 294 K and atmospheric pressure (1 bar). Water mist concentrations of 0.10, 0.20 and 0.32 kg/m^3 assuming a flow rate of 0.097 L/min at 50 bar and droplet size 19.5 µm were chosen to observe the effect on the laminar burning velocities of the mixtures. As expected, once water mist was injected into the chamber the visual capabilities with CPM was incapacitated, see Fig. 6.14. The interaction of a flame with water droplets including the effect of water mists on the flame propagation are therefore phenomena ruled out in the work of this thesis.

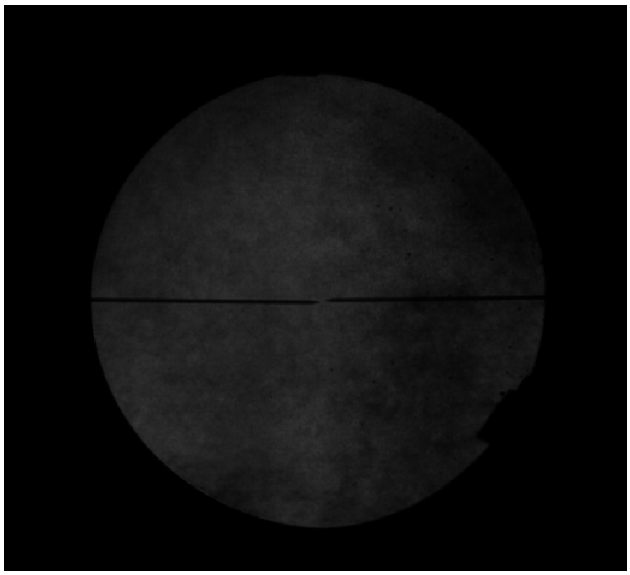

Figure 6.14: A schlieren image taken 0.5 seconds after water mist has been injected into the chamber, with the visibility already severely compromised.

When water mist is added to the hydrogen-air mixtures, the combustion develops into a two-phase reaction. The liquid water droplets undergoes a phase change into vapour, and in the process extracts energy from the system and lowers the value of p_{max}. The significance of water mist introduced to the hydrogen-air mixture combustion was first established by the effect on the experimental p_{max} and theoretical $p_{max,ad}$ values calculated using CEC. Taking only into account the effect of water mist concentrations added to the other gas reactants specified, Fig. 6.15 shows the results. Viewing the calculated $p_{max,ad}$ values, it is clear that by introducing water mist to a hydrogen-air mixture in a closed vessel reduces the final maximum pressure produced in a closed vessel. The reduction increases with water mist concentration and equivalence ratio, with a maximum relative difference of 1.5 bar at the richest mixture.

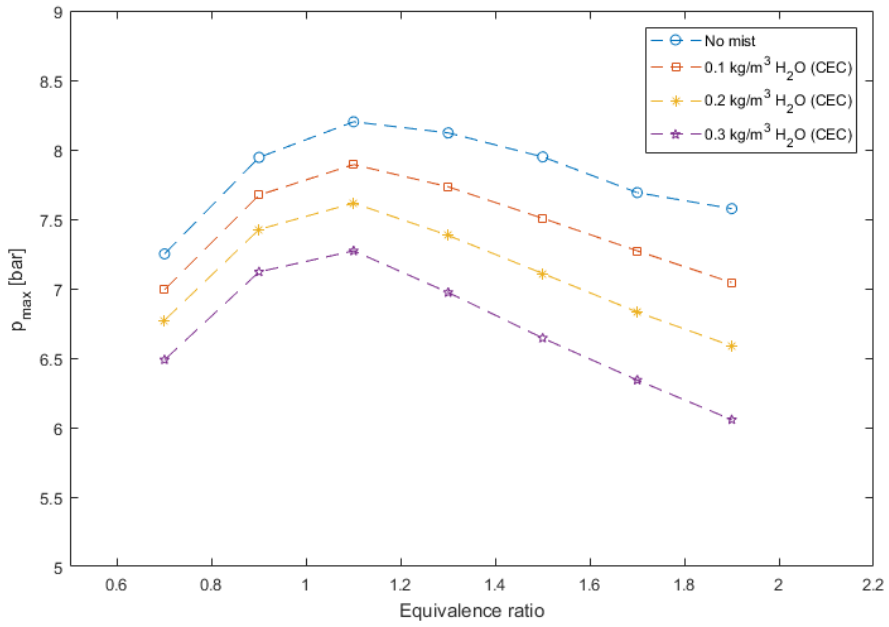

Figure 6.15: Using CEC, the calculated maximum pressure for water mist present in the initial hydrogen-air mixture are obtained with varying water mist concentrations.

The experimentally measured p_{max} however, does not show an equally clear trend contingent by the water mist concentrations. Although the obtained values were lower than when water mist was absent, a fluctuating trend is shown, independent of the water mist concentration above stoichiometric mixtures presented in Fig. 6.16.

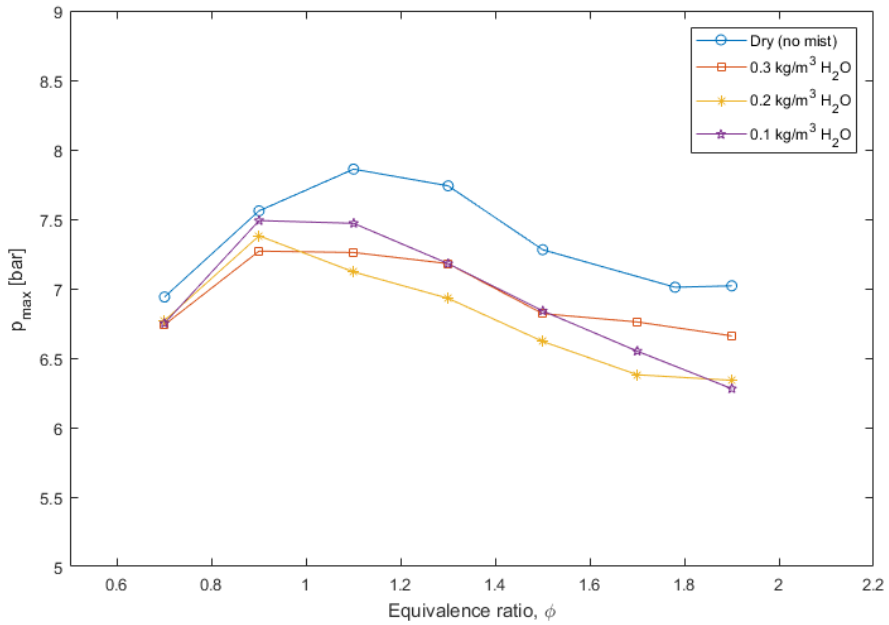

Figure 6.16: The experimentally found maximum pressures for water mist present in the initial hydrogen-air mixture, with varying water mist concentrations.

Using the CEC values of $p_{max,ad}$ to obtain the laminar burning velocities for consistency sake, the results are given in Fig. 6.17. First to notice, all three mixtures with varying water mist concentrations show burning velocities much higher than those obtained from the dry test. Especially for the water mist concentration of 0.3 kg/m^3, around a 100 % increase in the laminar burning velocity is attained across all mixtures, contradicting the natural mitigating effect of the water mist on the flame propagation.

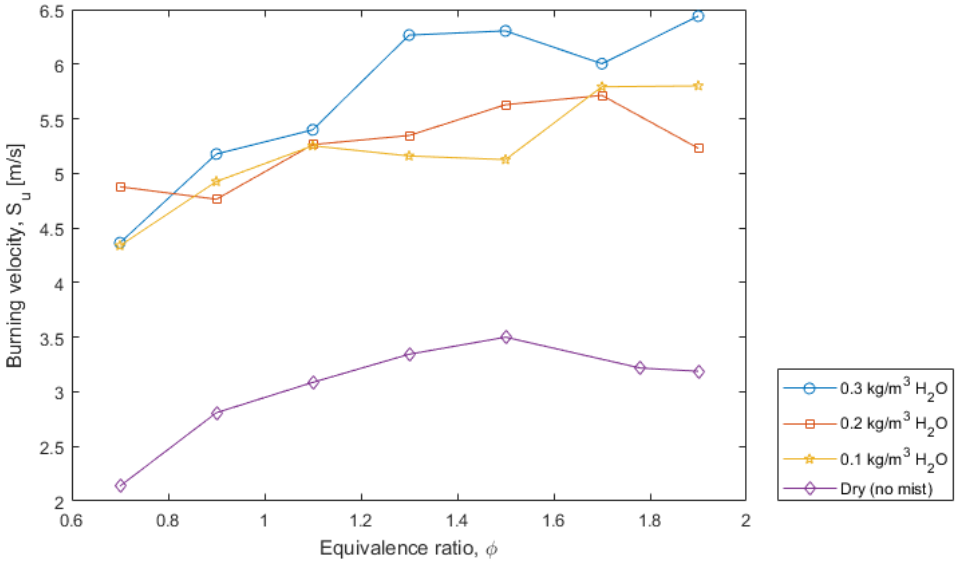

Figure 6.17: Comparison of estimated burning velocity measured with the introduction of water mist with various concentrations.

Intuitively, these findings implies an influence to the burning velocity beyond the scope of a laminar flow. Given the procedure executed as described in Sec 4.5.3, two areas of possible significance stand out. Initially, no latency between water mist injection and ignition was applied, for the water mist to first become quiescent. The second source related to the water mist concentration and droplet size distribution injected into the explosion chamber. During the injection of water mist, the pressure upsurge from the water reservoir to the chamber happens simultaneously as the pressurised water was being injected through the nozzle, producing a wide spectre of water droplet SMDs and water mist concentration. These two implications are the subject of the next two subsections.

6.3.1 Water mist concentration and droplet characteristics

The manufacturer of the nozzle, Hansa Engineering AS, ran simulations to determine the SMD for the nozzle depending the fluid pressure through the nozzle. Fig. 6.18 show the SMD decreasing from 32 µm at 10 bar to 16.9 µm at 80 bar. In other words, the higher the p_{nozzle} operated with, the smaller the water mist droplets manufactured become.

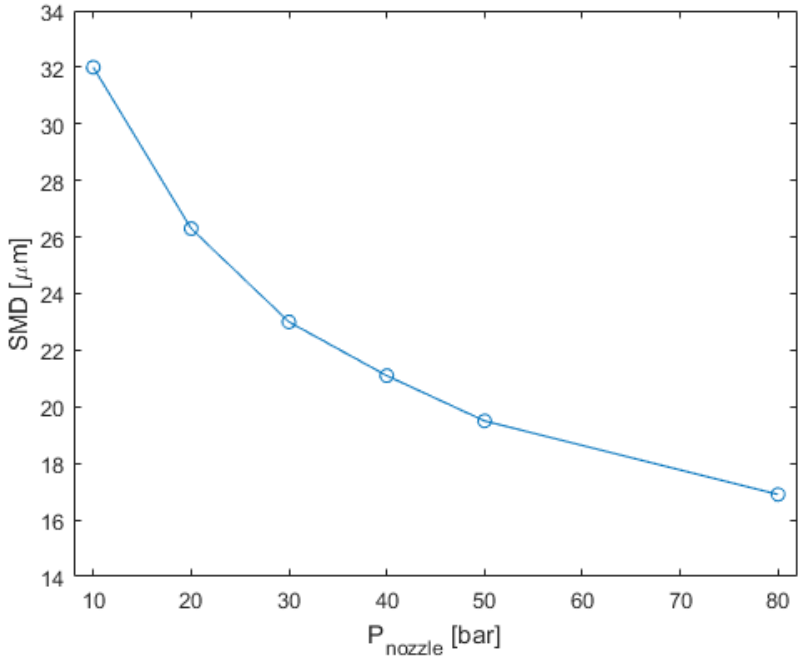

Figure 6.18: Tabulated SMD distributions generated through pressure atomization, provided by the manufacturer Hansa Engineering AS.

An empirical method of measuring the pressure (p_{nozzle}) upsurge time duration from 0-50 bar was conducted to determine the actual concentration injected. These values were then used to calculate the flow rate using Eq. (4.3) Both trends are illustrated in Fig. 6.19. p_{nozzle} reaches 50 bar after 1.86 seconds, corresponding thereafter to a constant flow rate of 0.0016 litre/s. Averaging the flow rate between each time step as function of duration injected, the actual water mist concentration was calculated, departing from the assumption of a constant flow rate. New water mist concentrations were found corresponding to the time duration of water mist injection of 1.3, 2.5 and 4 seconds, presented in Tab. 6.2. The difference in assumed and calculated water mist concentrations, being a reduction of only 0.02 kg/m^3 across all three mixtures, the assumption of the difference being exceeding is debunked. Nonetheless, the calculated values are used forward in this work.

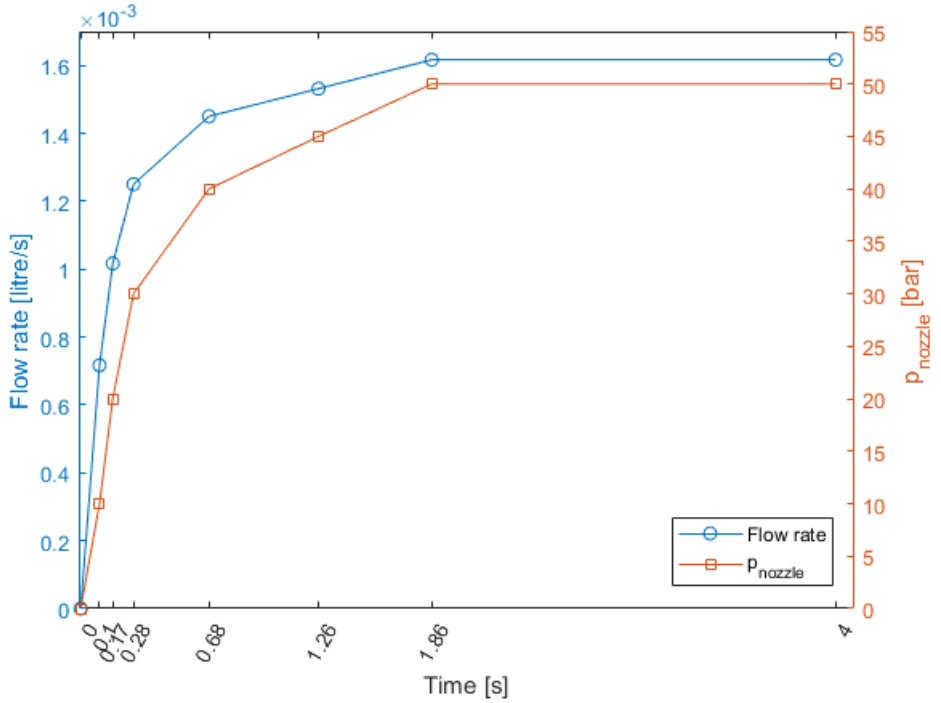

Figure 6.19: Flow rate injected into the chamber, found from the pressure (p_{nozzle}) duration needed for the highest concentration of water mist (0.3 kg/m^3).

Table 6.2: Assummed and calculated water mist concentrations based on the duration of p_{noxxle}, injecting water mist into the explosion chamber.

Duration of nozzle pressure (s)	Assumed concentration (kg/m^3)	Calculated concentration (kg/m^3)
1.3	0.10	0.08
2.5	0.20	0.18
4	0.32	0.30

Constraints in the experimental work concerning both nozzle (minimum SMD $>$ 11 μm) and the compressed-air regulator (maximum outlet pressure = 50 bar) led to a minimum water mist SMD of 19.5 µm. In addition, the nozzle pressure upsurge would also vary the atomization of water droplets and as a result, create a polydisperse droplet size distribution pertaining each concentration. With the SMD for each pressure outlined in Fig. 6.18, and knowing the time duration between each pressure, Fig. 6.20 show pie charts representing the calculated actual droplet size distribution for each

concentration. Clearly, the SMDs for each concentration are heavily influenced by the dynamic p_{nozzle}. In general, droplet sizes marginally larger than the upper limit of 10 µm for a full evaporation is evident [39].

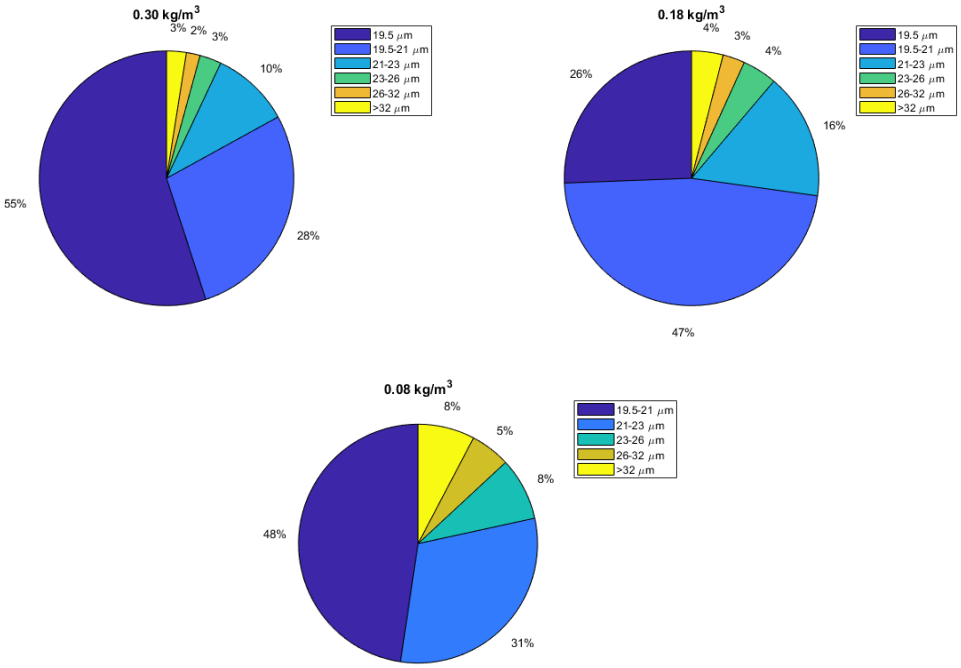

Figure 6.20: Pie charts displaying the injected water droplet SMD distribution, based on the dynamic pressure injected, p_{nozzle}.

Droplet break-up takes place when strong enough hydrodynamic forces due to strong flows around the droplet occurs. This depends on the congesting factor of the area, if strong flame and flow accelerations takes place. The range of SMD, whereby a droplet break-up to take place, is according to van Wingerden et al. [39] above 200-250 µm, and consequently not an possible occurrence in this case. As turbulence was generated by the system overriding the influence of the droplet size, further tests to determine the decrease of effectiveness as function of the droplet size was unwarranted. An attempt was made with the already available high-speed camera to determine the water droplet size and velocity, to no avail. The experiment is outlined in Appendix B.

6.3.2 Water-spray-generated turbulence

Turbulence, in contrast to a laminar flow regime, is characterized by chaotic changes in both pressure and flow velocity. The generation of turbulence is highly dependent on the critical velocity, after which point demises laminar motion flow, moving erratically in form of cross-currents and eddies [18]. These cross-currents and eddies, with an increased effective surface area, gives rise to nominal turbulent burning velocities that can be considerably higher than the laminar values for the same gas mixture. Accordingly, as the water mist was injected into the chamber with a flow rate assumed above the critical velocity, turbulence was likely to appear and thereby increase the burning velocity as seen in Fig. 6.17.

Turbulence theory is beyond the scope of this thesis and therefore, the strive to quantify the generated turbulence is forfeited. Issues dealing with the characteristics of the nozzle concerning the orifice dimensions and flow velocity requires thorough investigation before determining quantities such as the Reynolds number and decay time of isotropic turbulence. An effort was nevertheless made to estimate the duration of time needed for the water mist to become quiescent enough to measure the laminar burning velocity. The latency stimulates decay of the turbulence intensity, and could allow the water droplets to successfully act as a heat sink to the propagating flame. This would however also lead to perceivable less water mist concentration still airborne due to gravity, as the latency increases before ignition resulting in less interaction between water mist and flame propagation. Time delays of ignition up to 240 seconds with a fixed equivalence ratio of $\phi = 1.1$, 0.30 kg/m^3 H_2O and ambient temperature were tested to examine the effect. Still, as observed in Fig. 6.21, all measured burning velocities remain higher than the dry test measured laminar burning velocity of 3.09 m/s.

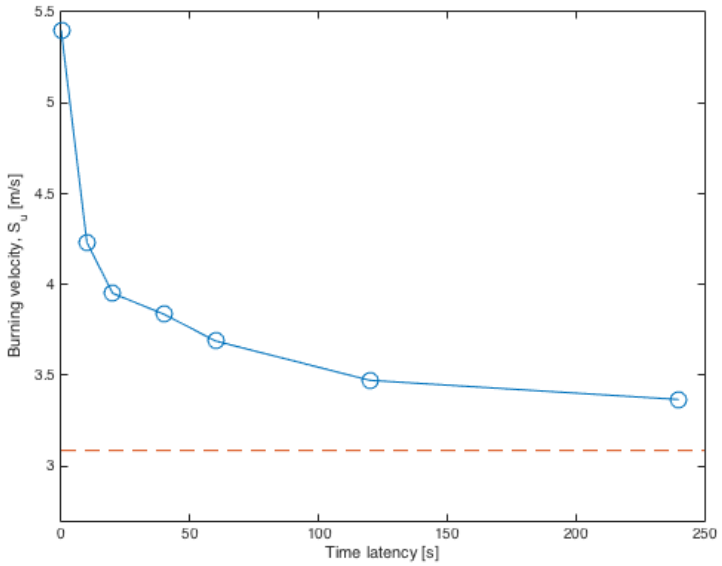

Figure 6.21: Burning velocities of hydrogen-air mixture ($\phi = 1.1$), showing the effect of varying the time between water mist injection (0.30 kg/m^3 H_2O) and moment of ignition. The dashed line represents the burning velocity obtained without water mist present.

Tests with a chosen latency period of 40 seconds covering the remaining equivalence ratios were employed to observed the effect on a broader scale, see Fig. 6.22. It was again clear that with an increased latency period, the water mist became more quiescent and consequently resulted in lower laminar burning velocities compared to burning velocities without latency. All the same, it was still apparent that the burning velocities were relatively higher compared to the dry tests with about 50 % increased burning velocity at most ($\phi = 1.9$). The tests with 40 seconds latency was also observed to have less scattering, and velocities at $\phi = 0.7$ and 0.9 produced lower values compared to the dry tests. These two aberrations substantiates the bulk flow source of turbulence made by van Wingerden and Wilkins [43], as it occurs when the concentration of water mist is low. A lower bulk concentration given adequate time to become quiescent would possess less momentum, influencing the burning velocity in a lower degree.

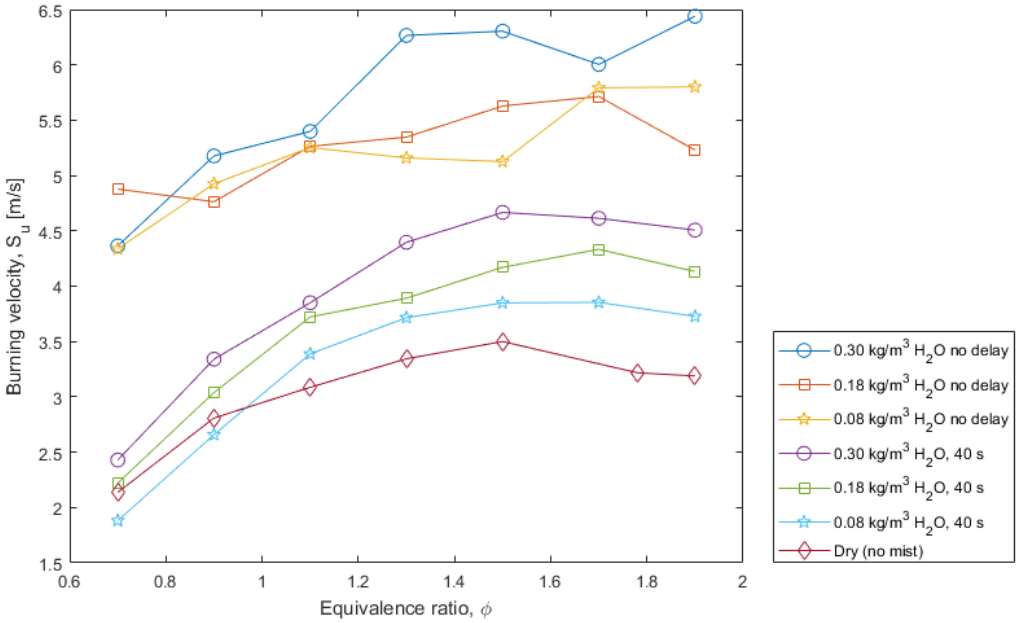

Figure 6.22: Comparison of estimated burning velocities of various amount of water mist, and ignition with and without 40 s latency.

6.4 Exploring experimental uncertainties

As with any research paper, a thorough investigation into the source of errors, and an estimation of the influence perceived on the final result, is imperative.

6.4.1 Uncertainty from chamber design

As the flame propagates through the enclosure, the pressure was assumed to be uniform in space, compressing both the unburned and burned gases. Eq. (2.19) is also independent of the shape of the vessel used, as long as the confinement issues are considered. However, in the unique case of a cubical enclosure used as in the work of this thesis, its effect had not been qualitatively explained or quantitatively determined, detailing how chamber geometry, pressure-release timing and exact range used for extrapolation may affect the burning velocity. Though it is not the aim of this thesis to do so, a brief exploration is done.

Uniform propagation of the spherical flame and corresponding pressure rise in a cubical enclosure is beyond the bonds of possibility. The initial spherical flame will eventually become increasingly cubical in shape as the distance from the centrally ignited flame front to the walls will vary, illustrated in Fig. 6.23. In addition, secondary flows in the corners of the cubical vessel may arise, causing a contrasting effect on the overall flow pattern. This may have significant implications on determination of planar flame speeds, and implies a more restrictive data reduction.

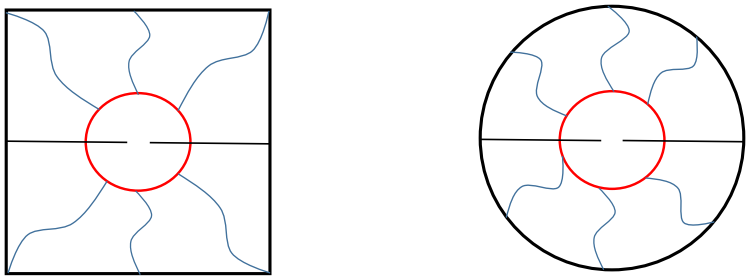

Figure 6.23: The flame and pressure distribution, non-uniform in a cubic enclosure and uniform in a spherical enclosure.

In determining the laminar burning velocity with the expanding flame front, an assumption of constant pressure was ensured. However, the unburned gas ahead of the flame front is mobilized and depending on the the interaction with the wall nearest to it, it may cause uniformity in the flame front due to the chamber confinement. Quantifying the uncertainty of flow field caused by non-spherical confinement was done by Burke et al. [49], using a cylindrical test chamber. He detected that the deviation from the assumed flow field caused significant errors in the instantaneous flame speed measurements, which were amplified in the extrapolation to zero stretch rate when using the constant-pressure method. He furthermore observed that the cylindrical pipe compressed the wave front progressing into an elliptical shape. In the view observed in schlieren images, the flame front would still appear circular, but propagate at a lower rate of E-1 for hydrogen fuels in air. This contradicts the behaviour of results found in this thesis, which show much higher velocities compared to the literature. Still, correction factors for cubical bomb measurements are warranted.

6.4.2 Uncertainty from system optics

An asymmetrical shape of the flame due to the electrodes or alignment bias, might lead to uncertainty extrapolating the flame velocity. On average, the total number of pixels determining the radius within the valid range of extrapolation was at 20-200 pixels. A deviation of maximum 5% constitutes 2-10 pixels added or subtracted to the flame diameter corresponding to 0.8-2 cm flame diameter. Uncertainty induced with the calibration factor and correct edge detection could be an additional source of uncertainty, with a pixel added to the range of pixel-deviation. Calculating the total effect it might have on the burning velocity, a hydrogen-air mixture at stoichiometry was adjusted with alternated flame radius, added and subtracted from the established valid range of extrapolation, 11-40 mm. The outcome was a laminar burning velocity average deviation of $\pm$ 0.3 m/s. This was significant enough to be considered as a potential source or error.

6.4.3 Uncertainty from the pressure measurement

Pressure range

In the pressure data processing, different ranges of pressure history are used by various authors without any clarification to how this range affects the accuracy of the laminar burning velocity. Although the maximum range of pressure is somewhat agreed upon at the inflection point, the lower bound within the measuring range differ. For example, Razus et al. [60] suggested to use data at $p_0 > 1.5$ bar to avoid disturbing effects of flame stretch and curvature on normal burning velocity during this stage. For three chamber sizes, Xiouris [61] computationally indicated that for values of $p_0 > 2.5$ bar stretch effects were reduced to very small values. Chen et al. [48] observed that the stretch effect on flame speed was greater than 10% when the pressure increase was below 20% of the initial pressure. The cases of both lowered and increased pressure range were explored and presented in Fig. 6.24, for a mixture of $\phi = 1.5$. A velocity of $S_{u_0} \pm 0.5$ m/s was observed when the lower pressure range bound was varied 1.5-2.5 bar.

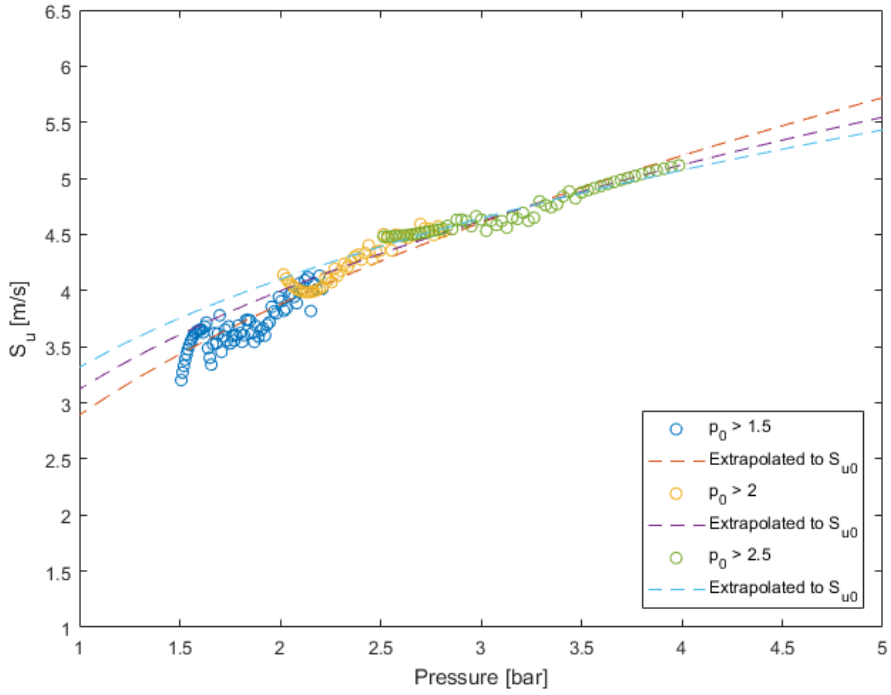

Figure 6.24: Varying the lower pressure range of measured pressure used to calculate and extrapolate the laminar burning velocity, at $\phi = 1.5$.

Extending the lower pressure bound on the remaining mixtures was explored, presenting the margin of uncertainty as error bars in Fig. 6.25. A huge range is covered for each mixture, with bars above the obtained velocities being most prominent with a maximum relative difference of 0.91 m/s at the richest mixture $\phi = 1.9$. The bars below the obtained burning velocities are however modest, and does not encapsulate the lower laminar burning velocities found in other literature. Nevertheless, this reaffirms the uncertainties related to the different pressure ranges chosen and its effect on the laminar burning velocities extrapolated at initial reference conditions.

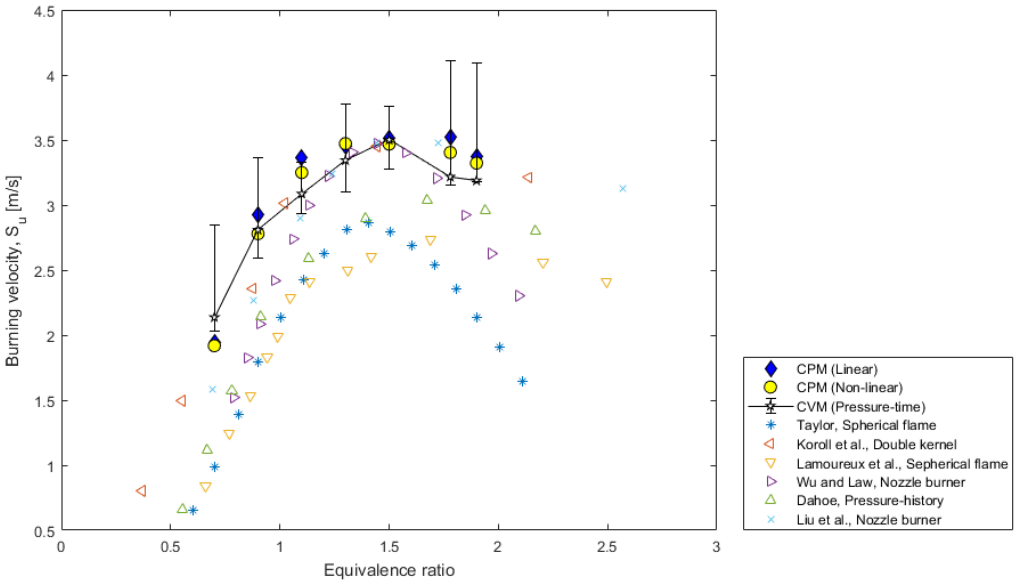

Figure 6.25: Different extrapolation ranges for the measured pressure (p_0 = 1.5, 2, 2.5) used in calculating S_{u_0} compared to laminar burning velocities measured in this work and in other literature.

Initial pressure

Extremely important for the constant-volume method of determining the laminar burning velocity, is reproducing identical initial pressure, as a reference point. In addition, a higher initial pressure has an aiding effect on the flame propagation of hydrogen-air mixtures [62]. A constant atmospheric pressure of 1 bar was assumed throughout the tests conducted when initially filling the explosion chamber. An investigation into the general air pressure in Bergen during a span of the testing period was done, with a wish to see if the assumption held true. Continuously monitored by the geophysical institute at UoB [63], Fig. 6.26 shows pressure variations during a week. With pressure varying between 0.970-1.0015 bar, the influence on the laminar burning velocity was calculated and concluded minimal, with margin of error $\pm$ 0.0004 m/s across all equivalence ratios.

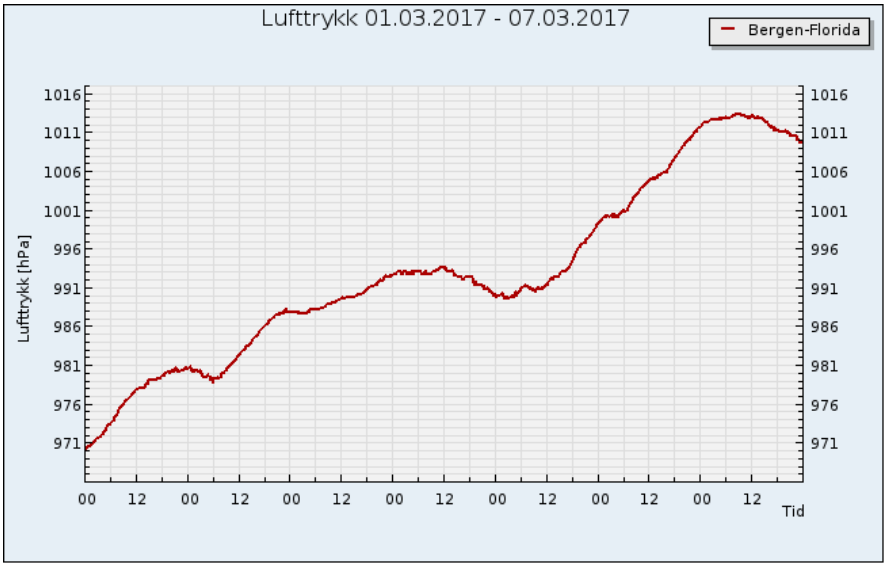

Figure 6.26: Air pressure (hPa) measured at Florida, Bergen between 01.03.2017 - 07.03.2017.

6.4.4 Initial temperature variation

The assumed ambient temperature of 294 K was subject to small changes, which was investigated to see its effect. This is because higher initial temperatures always promote the faster flame propagation [62]. Influence from temperature variation was considered as there were no thermocouples installed in the chamber to monitor any variation of temperature prior to ignition. Expansion ratios using CEC were calculated for a hydrogen-air mixture at stoichiometry, changing the initial temperature to quantify the effect it might have on the determination of the burning velocity. Choosing an area of temperature from 279-304 K, the effect is illustrated in Fig. 6.27. A variation in initial temperature of 25 K gave a corresponding change of 0.3 m/s. With certainty that the temperature fluctuations during testing were well within $\pm$ 3 K, this was not considered a major source of error.

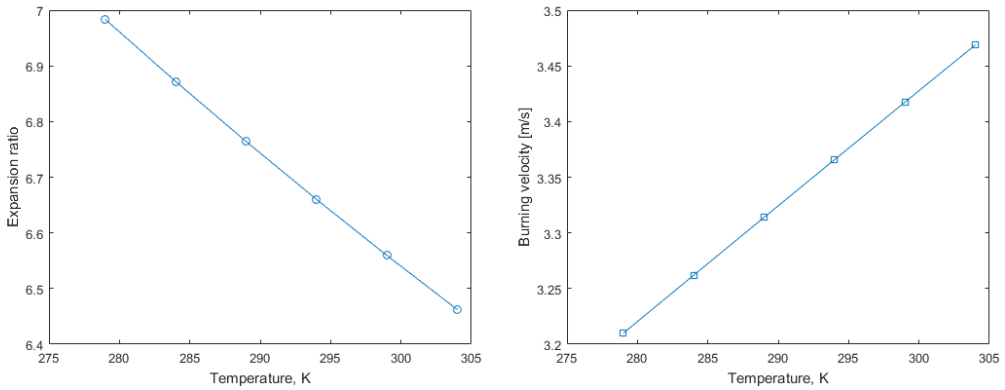

Figure 6.27: Variation in the expansion ratio and burning velocity with initial temperature.

6.4.5 Gas mixture discrepancy

Uncertainty corresponding to imperfect vacuum, and precision of the the employed partial pressure were pointed towards the single manometer used. As mentioned in Sec. 4.5.1, the final mixture recorded was based on the measured partial pressures of fuel and air. This eliminated most of the uncertainty involving the equivalence ratio prior to ignition. According to the manufacturers data sheet the measuring error of the pressure sensor was 0.1% with full scale accuracy. With an already 0.1 mbar gauge readout resolution, this contribution on the measured burning velocity was therefore considered negligible.

6.4.6 Uncertainty associated with experiments done with hydrogen-air mixtures exposed to water mist

Uncertainty related to measurements done with the pressure-time history method is already outlined in Sec. 6.4.3. Additional uncertainties connected to the addition of water mist are outlined below.

Calculating the final maximum pressure

By calculating S_{u_0} for hydrogen-air mixtures exposed to water mist including values found using CEC, it assumed the fact that all the liquid water droplets

were evaporated into water vapour in the final product. The maximum pressures calculated were therefore the upper bound $p_{max,ad}$, and in reality might be lower. As mentioned in Sec. 6.2.2, a lower maximum pressure leads to a higher calculated burning velocity which sets the already elevated obtained values even higher. Contradicting a possible consolidation between the obtained burning velocities, with and without water mist, an effort to quantify this uncertainty was omitted.

Inhomogeneous dispersion of water mist

Due to an inhomogeneous water mist trajectory from the nozzle, see Fig. 6.28, a corresponding registered uneven flame propagation monitored by the pressure transducer was most likely due to its stationary position in the chamber. This may be the cause of scatter in the initial results, without latency between injection of water mist and ignition. The absence of visual observation of the flame forfeited the possibility to observe possible factors such as flame speed uniformity, and likely predominant direction of flame speed increase.

Figure 6.28: Water mist trajectory from the water nozzle at the outset.

Chapter 7

Conclusion

Experimental determination of laminar burning velocities of premixed hydrogen-air mixtures using the constant-pressure method (CPM), and the constant-volume method (CVM) was obtained. Using the CPM method, a schlieren optical system was used to measure the stretched flame speeds. Linearly and non-linearly, the unstretched flame speeds were extrapolated and the laminar burning velocities were calculated. Employing CVM, the laminar burning velocities were obtained from the measured pressure-time histories, relating the dynamic pressure rises to the flame propagations. Comparing the results acquired by CPM and CVM, equitable agreement was attained, with an utmost deviation of 10 % in laminar burning velocity. Comparing the laminar burning velocities to those available in the literature, the velocities obtained in this work were higher in magnitude for all seven mixtures.

Using CVM, hydrogen-air mixtures were introduced to water mist with concentrations of 0.08-0.30 kg/m^3. While the original motivation for the introduction of water mist was to see its mitigating effect on the laminar burning velocity, this was quickly counteracted with turbulence engender resulting in obtained burning velocities twice the values. Turbulence generated from the water mist bulk momentum after injection superseded the waters ability to act as a heat sink within the flame. Latency between injection of water mist and ignition lowered the burning velocities, but not below those obtained without water mist, still increased with 50 % at most. An attempt to identify sources of errors in the obtained values for laminar burning velocities was conducted, citing the hydrodynamic instabilities, post-processing uncertainty, and cubical chamber-design influence as possible sources.

Chapter 8

Further study

Significant changes and optimization are needed in order to obtain acceptable results for the burning velocities measured using both the CPM and CVM:

- A larger vessel with a spherical shape to maximize the relatively unaffected region of data allowing for a more straightforward approach to interpret the experimental data.
- An adjustable ignition energy varying the spark energy to access the influence of the early-stage, ignition-affected flame evolution. This would help determine a more correct lower bound extrapolation point. A gas analyser could be implemented for more accurate gas mixture composition and mixing before ignition.
- An effort to study and quantify the turbulence generated by the water mist induced flow would be useful. Subsequently, a different nozzle type, i.e. a bi-fluid nozzle, that can produce SMDs < 10 µm would then be beneficial to determining its mitigating influence on the flame.

Additional research might then be implemented, such as having thermocouples installed inside the vessel to provide information about the temperature inside. This would open for higher initial mixture temperature, in addition to steam insertion inside the vessel.

References

[1] Sikkerheitsteknologi / Process safety technology | University of Bergen. http://www.uib.no/en/studyprogramme/MAMN-PRO/SI#uib-tabs-introduction, 2017. [Online; accessed January-2017].

[2] Gexcon AS - DSEAR, Fire and Explosion Consultants. https://www.gexcon.com/about, 2017. [Online; accessed January-2017].

[3] J. Warnatz, U. Maas, and Robert W. Dibble. *Combustion: physical and chemical fundamentals, modeling and simulation, experiments, pollutant formation.* Springer, Berlin ; New York, 4th ed edition, 2006.

[4] Roy Nersesian. *Energy for the 21st Century: a Comprehensive Guide to Conventional and Alternative Sources.* Taylor and Francis, Hoboken, 2014.

[5] Z.-G. Yang, Y. Gong, and J.-Z. Yuan. Failure analysis of leakage on titanium tubes within heat exchangers in a nuclear power plant. Part I: Electrochemical corrosion. *Materials and Corrosion*, 63(1):7–17, January 2012.

[6] Tohru Mitani. A flame inhibition theory by inert dust and spray. *Combustion and Flame*, 43:243–253, January 1981.

[7] M. F. Ivanov, A. D. Kiverin, and M. A. Liberman. Flame acceleration and DDT of hydrogen–oxygen gaseous mixtures in channels with no-slip walls. *International Journal of Hydrogen Energy*, 36(13):7714–7727, July 2011.

[8] S. J. Jones, A. F. Averill, J. M. Ingram, P. G. Holborn, P. Battersby, P. F. Nolan, I. D. Kempsell, and M. J. Wakem. Mitigation of hydrogen-air explosion using fine water mist sprays. In *INSTITUTION OF CHEMICAL ENGINEERS SYMPOSIUM SERIES*, volume 151, page 440. Institution of Chemical Engineers; 1999, 2006.

[9] Abhijit U. Modak, Angel Abbud-Madrid, Jean-Pierre Delplanque, and Robert J. Kee. The effect of mono-dispersed water mist on the suppression of laminar premixed hydrogen–, methane–, and propane–air flames. *Combustion and Flame*, 144(1–2):103–111, January 2006.

[10] S. Paul Fuss, Ezra F. Chen, Wenhua Yang, Robert J. Kee, Bradley A. Williams, and James W. Fleming. Inhibition of premixed methane/air flames by water mist. *Proceedings of the Combustion Institute*, 29(1):361–368, January 2002.

[11] J. M. Ingram, A. F. Averill, P. N. Battersby, P. G. Holborn, and P. F. Nolan. Suppression of hydrogen–oxygen–nitrogen explosions by fine water mist: Part 1. Burning velocity. *International Journal of Hydrogen Energy*, 37(24):19250–19257, December 2012.

[12] C. A. Brebbia and P. Vorobieff. *Computational Methods in Multiphase Flow VII*. WIT Press, July 2013.

[13] Derek Bradley, P. H. Gaskell, and X. J. Gu. Burning velocities, markstein lengths, and flame quenching for spherical methane-air flames: A computational study. *Combustion and Flame*, 104(1):176–198, January 1996.

[14] A. E. Dahoe. Laminar burning velocities of hydrogen–air mixtures from closed vessel gas explosions. *Journal of Loss Prevention in the Process Industries*, 18(3):152–166, May 2005.

[15] Kari Halland. Measurements of laminar burning velocities in premixed gases by the schlieren imaging technique. Master's thesis, The University of Bergen, June 2015.

[16] F. A. Williams. Lectures on applied mathematics in combustion: Past contributions and future problems in laminar and turbulent combustion. *Physica D: Nonlinear Phenomena*, 20(1):21–34, May 1986.

[17] Jacqueline Akhavan. *The Chemistry of Explosives*. Royal Society of Chemistry Information Services, 1998.

[18] Rolf K. Eckhoff. *Explosion hazards in the process industries*. Gulf Pub, Houston, TX, 2005.

[19] Dougal Drysdale. *Wiley: An Introduction to Fire Dynamics, 3rd Edition*. John Wiley and Sons, Ltd, 2011.

[20] Bjørn Johan Arntzen. *Modelling of turbulence and combustion for simulation of gas explosions in complex geometries*. PhD thesis, Norges teknisk-naturvitenskapelige universitet, 1998.

[21] Thierry Poinsot and D. Veynante. *Theoretical and numerical combustion*. Edwards, Philadelphia, 2nd ed edition, 2005.

[22] A. P. Kelley and C. K. Law. Nonlinear effects in the extraction of laminar flame speeds from expanding spherical flames. *Combustion and Flame*, 156(9):1844–1851, September 2009.

[23] Ahmad Omari and Leonid Tartakovsky. Measurement of the laminar burning velocity using the confined and unconfined spherical flame methods – A comparative analysis. *Combustion and Flame*, 168:127–137, June 2016.

[24] Ernest F. Fiock and Charles F. Marvin. The measurement of flame speeds. *Proceedings of the Symposium on Combustion*, 1:194–205, January 1948.

[25] K. H. O'Donovan and C. J. Rallis. A modified analysis for the determination of the burning velocity of a gas mixture in a spherical constant volume combustion vessel. *Combustion and Flame*, 3:201–214, January 1959.

[26] C. C. M. Luijten, E. Doosje, and L. P. H. de Goey. Accurate analytical models for fractional pressure rise in constant volume combustion. *International Journal of Thermal Sciences*, 48(6):1213–1222, June 2009.

[27] G. S. Settles. *Schlieren and shadowgraph techniques: visualizing phenomena in transparent media*. Experimental fluid mechanics. Springer, Berlin ; New York, 2001.

[28] Amrita Mazumdar. Principles and techniques of schlieren imaging systems. *Columbia University, Department of Computer Science*, 2011.

[29] Jan R Lien, Egil Lillestøl, Ola Hunderi, and Gunnar Løvhøiden. *Generell fysikk for universiteter og høgskoler. Mekanikk Bd. 1 Bd. 1*. Universitetsforlaget, Oslo, 2001.

[30] Nicolas Degen. An overview on Schlieren optics and its applications. *ETH-Zürich*, 2012.

[31] G.S Speak and D.J. Walters. Optical Considerations and Limitations of the Schlieren Method. *Ministry of Supply, Aeronautical Research Council Reports and Memoranda*, page 27, 1954.

[32] Simon Crispin Taylor. *Burning velocity and the influence of flame stretch.* phd, University of Leeds, September 1991.

[33] G. E. Andrews and D. Bradley. Determination of burning velocities: A critical review. *Combustion and Flame*, 18(1):133–153, February 1972.

[34] Boris E. Gelfand, Mikhail V. Silnikov, Sergey P. Medvedev, and Sergey V. Khomik. Laminar and Cellular Combustion of Hydrogenous Gaseous Mixtures. In *Thermo-Gas Dynamics of Hydrogen Combustion and Explosion*, Shock Wave and High Pressure Phenomena, pages 15–51. Springer Berlin Heidelberg, 2012.

[35] C. K. Law. A Compilation of Experimental Data on Laminar Burning Velocities. In Norbert Peters and Bernd Rogg, editors, *Reduced Kinetic Mechanisms for Applications in Combustion Systems*, number 15 in Lecture Notes in Physics Monographs, pages 15–26. Springer Berlin Heidelberg, 1993.

[36] Zhigang Liu and Andrew K. Kim. A Review of Water Mist Fire Suppression Systems— Fundamental Studies. *Journal of Fire Protection Engineering*, 10(3):32–50, August 1999.

[37] P. N. Battersby, A. F. Averill, J. M. Ingram, P. G. Holborn, and P. F. Nolan. Suppression of hydrogen–oxygen–nitrogen explosions by fine water mist: Part 2. Mitigation of vented deflagrations. *International Journal of Hydrogen Energy*, 37(24):19258–19267, December 2012.

[38] H. Cheikhravat, J. Goulier, A. Bentaib, N. Meynet, N. Chaumeix, and C. E. Paillard. Effects of water sprays on flame propagation in hydrogen/air/steam mixtures. *Proceedings of the Combustion Institute*, 35(3):2715–2722, 2015.

[39] Kees van Wingerden, Brian Wilkins, Jørn Bakken, and Geir Pedersen. The influence of water sprays on gas explosions. Part 2: mitigation. *Journal of Loss Prevention in the Process Industries*, 8(2):61–70, January 1995.

[40] P. G. Holborn, P. Battersby, J. M. Ingram, A. F. Averill, and P. F. Nolan. Estimating the effect of water fog and nitrogen dilution upon the burning velocity of hydrogen deflagrations from experimental test data. *International Journal of Hydrogen Energy*, 38(16):6882–6895, May 2013.

[41] P. G. Holborn, P. Battersby, J. M. Ingram, A. F. Averill, and P. F. Nolan. Modelling the effect of water fog on the upper flammability limit of

hydrogen–oxygen–nitrogen mixtures. *International Journal of Hydrogen Energy*, 38(16):6896–6903, May 2013.

[42] Paul G. Holborn, Paul N. Battersby, James M. Ingram, Anthony F. Averill, and Philip F. Nolan. Modelling the mitigation of a hydrogen deflagration in a nuclear waste silo ullage with water fog. *Process Safety and Environmental Protection*, 91(6):476–482, November 2013.

[43] Kees van Wingerden and Brian Wilkins. The influence of water sprays on gas explosions. Part 1: water-spray-generated turbulence. *Journal of Loss Prevention in the Process Industries*, 8(2):53–59, January 1995.

[44] Trygve Skjold. Selected aspects of turbulence and combustion in 20-litre explosion vessels : development of experimental apparatus and experimental investigation. Master's thesis, The University of Bergen, 2003.

[45] Erlend Randeberg, Werner Olsen, and Rolf K. Eckhoff. A new method for generation of synchronised capacitive sparks of low energy. *Journal of Electrostatics*, 64(3):263–272, March 2006.

[46] Ryo Ono, Masaharu Nifuku, Shuzo Fujiwara, Sadashige Horiguchi, and Tetsuji Oda. Minimum ignition energy of hydrogen–air mixture: Effects of humidity and spark duration. *Journal of Electrostatics*, 65(2):87–93, February 2007.

[47] Daniel Pugh. *Combustion characterisation of compositionally dynamic steelworks gases*. PhD thesis, Cardiff University, 2013.

[48] Z. Chen, M. P. Burke, and Y. Ju. Effects of compression and stretch on the determination of laminar flame speeds using propagating spherical flames. *Combustion Theory and Modelling*, 13(2):343–364, March 2009.

[49] Michael P. Burke, Zheng Chen, Yiguang Ju, and Frederick L. Dryer. Effect of cylindrical confinement on the determination of laminar flame speeds using outwardly propagating flames. *Combustion and Flame*, 156(4):771–779, April 2009.

[50] S. Coronel, N. Bitter, V. Thomas, R. Mevel, and J.E. Shepherd. Non-linear Extrapolation of Laminar Flame Properties from Spherically Expanding Flames. *Western States Section of the Combustion Institute California Institute of Technology*, March 2014.

[51] Chemical Equilibrium Calculator. http://navier.engr.colostate.edu/~dandy/code/code-4/index.html, 2017. [Online; accessed April-2017].

[52] Rochelle Prescott. A Method of Correction of Astigmatism in Schlieren Systems. *Journal of the Aeronautical Sciences*, 18(1):69–69, 1951.

[53] X. Bao and F. Liu. Instabilities of Hydrogen/Air Outwardly Propagating Spherical Laminar Premixed Flames. In *2010 International Conference on Digital Manufacturing Automation*, volume 1, pages 849–852, December 2010.

[54] Zuohua Huang, Yong Zhang, Ke Zeng, Bing Liu, Qian Wang, and Deming Jiang. Measurements of laminar burning velocities for natural gas–hydrogen–air mixtures. *Combustion and Flame*, 146(1–2):302–311, July 2006.

[55] Kenneth L Cashdollar, Isaac A. Zlochower, Gregory M Green, Richard A Thomas, and Martin Hertzberg. Flammability of methane, propane, and hydrogen gases. *Journal of Loss Prevention in the Process Industries*, 13(3–5):327–340, May 2000.

[56] C. K. Wu and C. K. Law. On the determination of laminar flame speeds from stretched flames. *Symposium (International) on Combustion*, 20(1):1941–1949, January 1985.

[57] G. W. Koroll, R. K. Kumar, and E. M. Bowles. Burning velocities of hydrogen-air mixtures. *Combustion and Flame*, 94(3):330–340, August 1993.

[58] D. D. S. Liu and R. MacFarlane. Laminar burning velocities of hydrogen-air and hydrogen-air steam flames. *Combustion and Flame*, 49(1–3):59–71, January 1983.

[59] N Lamoureux, N Djebaili-Chaumeix, and C. E Paillard. Laminar flame velocity determination for H2–air–He–CO2 mixtures using the spherical bomb method. *Experimental Thermal and Fluid Science*, 27(4):385–393, April 2003.

[60] Domnina Razus, Venera Brinzea, Maria Mitu, Codina Movileanu, and Dumitru Oancea. Burning Velocity of Propane–Air Mixtures from Pressure–Time Records during Explosions in a Closed Spherical Vessel. *Energy & Fuels*, 26(2):901–909, February 2012.

[61] Christodoulos Xiouris, Tailai Ye, Jagannath Jayachandran, and Fokion N. Egolfopoulos. Laminar flame speeds under engine-relevant conditions: Uncertainty quantification and minimization in spherically expanding flame experiments. *Combustion and Flame*, 163:270–283, January 2016.

[62] Toshio Iijima and Tadao Takeno. Effects of temperature and pressure on burning velocity. *Combustion and Flame*, 65(1):35–43, July 1986.

[63] Geofysisk institutt (UiB) -Været i Bergen. https://veret.gfi.uib.no/, 2017. [Online; accessed May-2017].

[64] Bjarne Husted. *Experimental measurements of water mist systems and implications for modelling in CFD.* PhD thesis, Lund University, 2007.

Appendix A

Explosion data

Mixture compositions, for all 55 explosions analysed in the work of this thesis, are outlined. ϕ is the equivalence ration; E is the expansion ratio; $p_{max,ex}$ is the experimentally measured maximum pressure; T_b and $P_{max,ad}$ are the adiabatic equilibrium temperature and pressure respectively calculated using CEC; γ_u and γ_b are the calculated specific heat ratios, unburned and burned respectively.

Table A.1: Initial dry tests.

Test	ϕ	E	$p_{max,ex}$(bar)	T_b (K)	$p_{max,ad}$(bar)	γ_u	γ_b
1	0.7008	6.071	5.94	2940.0	7.2499	1.2875	1.2074
2	0.8977	6.768	6.56	2678.6	7.9448	1.2704	1.2011
3	1.1005	7.009	6.86	2779.9	8.2010	1.2551	1.1881
4	1.3002	6.857	6.74	2742.0	8.1212	1.2420	1.1795
5	1.5025	6.660	6.28	2667.9	7.9484	1.2303	1.1724
6	1.7809	6.400	6.01	2561.2	7.6912	1.2162	1.1640
7	1.8991	6.287	6.02	2514.2	7.5756	1.2109	1.1608

Table A.2: Tests with no latency between water injection and ignition, with 0.30 kg/m^3 water mist concentration.

Test	ϕ	$p_{max,ex}$ (bar)	T_b (K)	$p_{max,ad}$ (bar)	γ_u	γ_b
8	0.7016	5.75	2130.3	6.4896	1.2527	1.1992
9	0.9059	6.49	2389.0	7.1341	1.2337	1.1792
10	1.1025	6.47	2445.0	7.2675	1.2189	1.1671
11	1.3053	6.18	2323.4	6.9595	1.2064	1.1598
12	1.5025	5.84	2201.3	6.6439	1.1962	1.1541
13	1.7150	5.55	2080.2	6.3250	1.1869	1.1490
14	1.9014	5.28	1980.3	6.0577	1.1798	1.1450

Table A.3: Tests with no latency between water injection and ignition, with 0.18 kg/m^3 water mist concentration.

Test	ϕ	$p_{max,ex}$ (bar)	T_b (K)	$p_{max,ad}$ (bar)	γ_u	γ_b
15	0.7032	5.77	2230.0	6.7719	1.2638	1.2057
16	0.9013	6.38	2493.3	7.4258	1.2455	1.1862
17	1.1015	6.12	2571.0	7.6155	1.2302	1.1734
18	1.3059	5.93	2476.5	7.3830	1.2171	1.1654
19	1.5019	5.62	2274.2	6.8770	1.2064	1.1609
20	1.7037	5.38	2259.4	6.8312	1.1968	1.1539
21	1.9029	5.24	2165.9	6.5871	1.1887	1.1492

Table A.4: Tests with no latency between water injection and ignition, with 0.08 kg/m^3 water mist concentration.

Test	ϕ	$p_{max,ex}$ (bar)	T_b (K)	$p_{max,ad}$ (bar)	γ_u	γ_b
22	0.7008	5.74	2307.4	6.9920	1.2744	1.2121
23	0.9004	6.27	2582.0	7.6734	1.2563	1.1926
24	1.1076	6.26	2669.3	7.8905	1.2405	1.1793
25	1.3099	6.18	2600.5	7.7277	1.2274	1.1710
26	1.5051	5.82	2506.8	7.4981	1.2163	1.1646
27	1.7213	5.76	2404.3	7.2416	1.2057	1.1585
28	1.9006	5.66	2326.6	7.0437	1.1980	1.1539

Table A.5: Tests with various latencies between water injection and ignition, with 0.30 kg/m^3 water mist concentration.

Test	ϕ	$p_{max,ex}$ (bar)	T_b (K)	$p_{max,ad}$ (bar)	γ_u	γ_b	Latency (s)
29	1.1010	6.79	2446.8	7.2720	1.2190	1.1671	10
30	1.1031	6.87	2445.4	7.2684	12189	1.1671	20
31	1.1066	6.85	2444.7	7.2667	1.2187	1.1669	40
32	1.1010	6.82	2446.8	7.2720	1.2190	1.1671	60
33	1.1046	6.84	2446.2	7.2704	1.2187	1.1669	90
34	1.1010	6.73	2446.8	7.2720	1.2190	1.1671	120

Table A.6: Tests with 40 s latency between water injection and ignition, with 0.08 kg/m^3 water mist concentration.

Test	ϕ	$p_{max,ex}$ (bar)	T_b (K)	$p_{max,ad}$ (bar)	γ_u	γ_b
35	0.7008	5.87	2582.7	6.9920	1.2563	1.1925
36	0.9013	6.56	2582.7	7.6752	1.2563	1.1925
37	1.1005	6.75	2670.4	7.8928	1.2410	1.1796
38	1.3019	6.72	2670.4	7.7332	1.2165	1.1618
39	1.5019	6.62	2510.0	7.5060	1.2165	1.1647
40	1.7009	6.35	2416.4	7.2719	1.2067	1.1590
41	1.8998	6.12	2326.6	7.0437	1.1980	1.1539

Table A.7: Tests with 40 s latency between water injection and ignition, with 0.18 kg/m^3 water mist concentration.

Test	ϕ	$p_{max,ex}$ (bar)	T_b (K)	$p_{max,ad}$ (bar)	γ_u	γ_b
42	0.7000	5.63	2225.1	6.7593	1.2641	1.2060
43	0.9018	6.45	2494.0	7.4275	1.2454	1.1861
44	1.1020	6.72	2571.4	7.6164	1.2302	1.1733
45	1.3025	6.74	2478.2	7.3874	1.2173	1.1655
46	1.5000	6.45	2367.5	7.1089	1.2065	1.1594
47	1.7030	6.37	2264.5	6.8444	1.1969	1.1539
48	1.9045	6.19	2165.9	6.5871	1.1887	1.1492

Table A.8: Tests with 40 s latency between water injection and ignition, with 0.30 kg/m^3 water mist concentration.

Test	ϕ	$p_{max,ex}$ (bar)	T_b (K)	$p_{max,ad}$ (bar)	γ_u	γ_b
49	0.7008	5.71	2129.4	6.4872	1.2527	1.1993
50	0.9004	6.43	2383.5	7.1207	1.2341	1.1797
51	1.1010	6.73	2446.8	7.2720	1.2190	1.1671
52	1.3002	6.72	2328.5	6.9724	1.2067	1.1600
53	1.5019	6.47	2201.3	6.6439	1.1962	1.1541
54	1.7016	6.23	2086.3	6.3414	1.1874	1.1493
55	1.9006	6.18	1979.8	6.0564	1.1798	1.1451

Appendix B

Experimental determination of water mist characteristics and behaviour

A cubical vessel in plexiglas, with replica dimensions as the explosion chamber used in this work, was constructed to gain full visible access to the characteristics and behaviour of the water mist, once introduced to the vessel. The purpose was to employ techniques for measuring velocity and droplet size using optical methods. Preferred to mechanical methods such as drop freezing and molten wax techniques, optical methods are non-intrusive whereby droplet size can be measured without interfering with the flow [64]. These methods include:

- Particle Image Velocimetry (PIV)
- Phase Doppler Anemometry
- Laser Diffraction
- High-speed camera

The three first methods were inapplicable due to lack of equipment, so the method using the already available high-speed camera was chosen. The principle involved determining the velocity and individual droplets from pictures taken directly of the mist during injection. Using the triggering system, this was easy to implement with images taken within the initial water mist injection period. While analysing the images afterwards, it was quickly apparent that this method, only utilizing a high-speed camera would not

yield in any tangible results as several disadvantages transpired. An image after 10 ms of injection period is displayed in Fig. B.1.

Figure B.1: Onset of water mist behaviour, 10 ms after injection with a flow rate of ≈ 0.031 l/min.

For a droplet size of around 20 µm in diameter, a minimum of four pixels would be needed to determine its, each covering a quadrant of the droplet. Each pixel would have to be approximately 10 µmm, the length of a radius. In pixel-to-cm ratio terms, 0.1 pixels/µm, or 1000 pixels/cm would be the minimum resolution needed to successfully detect a droplet and determine its size and velocity. This could be solved by imaging magnification within a 1 mm^2 region, but no such advanced equipment was available. In addition, in a dense spray it would be difficult to distinguish between the individual droplets. Ideally a single droplet would be injected and the size and velocity determined accordingly. Other configurations were lacking such as an ample light source, a laser to provide sufficient brightness and a software algorithm to correlate the images permitting both velocity and droplet size.

Nonetheless, visual aid was still used to observe the duration needed for the mist to settle. A series of pictures was taken of the replica vessel with a timer,

starting immediately after injection up until 4.06 min (246 s) presented in Fig. B.2. Although not that deductible illustrated by the images, a somewhat homogeneous mixture of water mist was first observed with a lot of movement. After 66 seconds, a more quiescent water mist behaviour was noticed, although the water mist could already be seen to gravitate towards the bottom. At 126 s and 246 s, with water mist adhering to the plexiglas wall, most of the water mist had gravitated at the bottom of the vessel. Methods of determining the water mist concentration after each time step was to be implemented, but was in the end not carried out. Ideally, a plate at the bottom able to accumulate the water settled, could be weighted to determine the concentration still airborne as a function of latency.

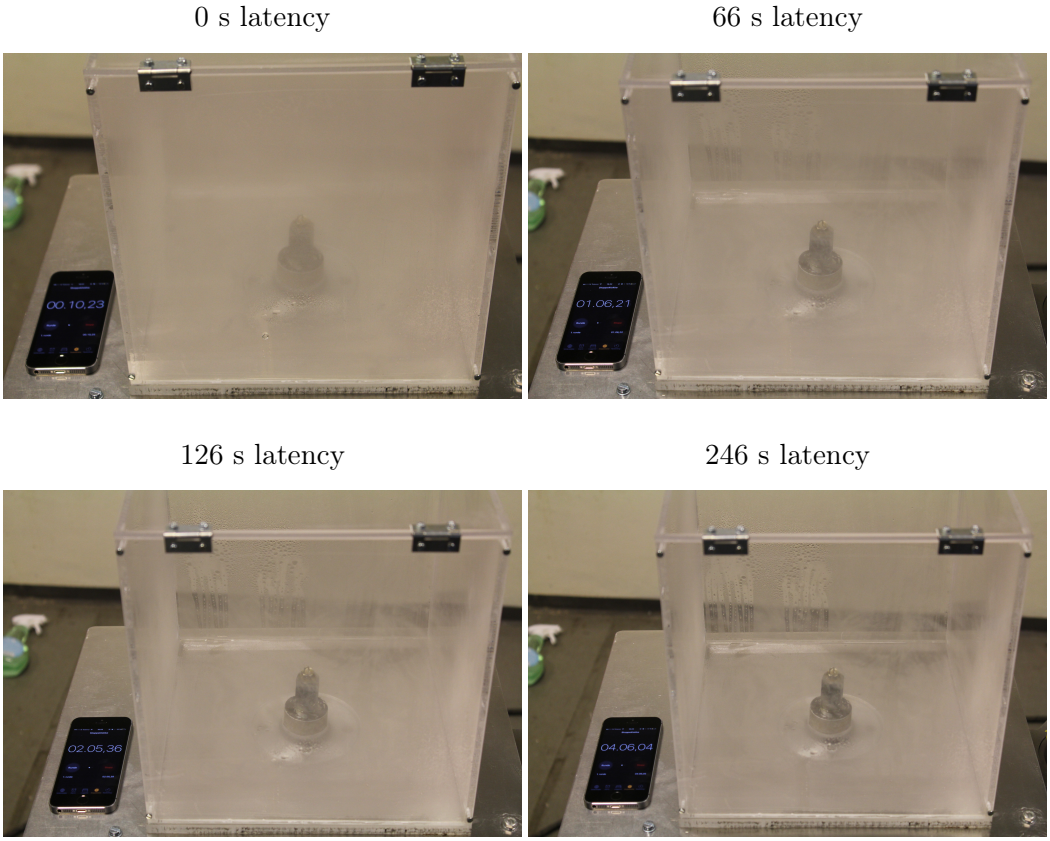

Figure B.2: A series of photograph showing the different latency effects of water mist behaviour in a cubical vessel after injection.